Bulletin of Volcanology (2025) 87:13
https://doi.org/10.1007/s00445-025-01797-1

RESEARCH ARTICLE

Dynamics of the 1873 CE "Breccia De Fiore" phreatic eruption at Vulcano (Aeolian Islands, Italy) through historical chronicles, physical volcanology, and numerical modelling

Silvia Giansante[1] · Tomaso Esposti Ongaro[1] · Raffaello Cioni[2] · Marco Pistolesi[1,3] · Mattia de' Michieli Vitturi[1]

Received: 24 June 2024 / Accepted: 19 January 2025

Abstract
Phreatic events may represent precursors of magmatic eruptions or occur independently as single or multiple episodes at volcanoes with hydrothermal systems. We examine the Breccia De Fiore deposit from the prolonged phreatic activity during September–October 1873 at the La Fossa cone of Vulcano (Aeolian Islands, Italy). By integrating data from historical chronicles, stratigraphy, sedimentology, physical analyses, and 3D numerical simulations, we investigate eruption dynamics. The sedimentological characteristics of the deposits, asymmetrically dispersed along the north-western flank of the cone, are interpreted as the simultaneous emplacement of pyroclastic density currents and ballistic projectiles. Numerical simulations model the eruptive mixture as an Eulerian gas-particle fluid coupled with Lagrangian ballistic particles. Results suggest the deposit originated from multiple, shallow, low-magnitude explosions ($<5\times10^4$ m^3 cumulative volume). The deposit dispersal is well reproduced by simulating explosions from an inclined vent, driven by pressure build-up (up to 5 MPa) at shallow depths (< 150 m) within the hydrothermal system. This study helps constrain critical parameters of phreatic scenarios at La Fossa volcano, including erupted mass and specific energy, emphasising the hazards posed by such small events and the crucial need for improving hazard assessment, especially given the close presence of populated, touristic sites.

Keywords Phreatic eruption dynamics · Vulcano Island · Pyroclastic density currents · Ballistic fallout · Numerical modelling · Hazard

Introduction

Vulcano Island (38° 24′N, 14° 58′E, 22 km^2) is an active volcanic centre in the southernmost sector of the Quaternary Aeolian arc (Tyrrhenian Sea, Italy; Fig. 1). Renowned for its distinctive "Vulcanian" eruptions (Clarke et al. 2015), it also hosts an active hydrothermal system, which manifests through a high-temperature fumarolic field, extensive CO_2 soil degassing, and rock alteration (Fulignati and Sbrana 1998; Di Giuseppe et al. 2023; Federico et al. 2023).

Since the last eruptive cycle in 1888–1890, activity has been characterised by continuous fumarolic outgassing, concentrated at the summit of the La Fossa cone and Porto di Levante area (Fulignati et al. 2006; Paonita et al. 2013; Federico et al. 2023). Several unrest episodes over the past century have been attributed to changes in heat and fluid supply to the hydrothermal system and permeability variations of host rocks (e.g., Badalamenti et al. 1988, 1991; Barberi et al. 1991; Chiodini et al. 1995; Diliberto et al. 2002; Harris et al. 2012; Paonita et al. 2013; Federico et al. 2023). The first recorded episode in 1916 saw increased gas flux and temperatures (up to 416 °C) in the fumaroles of the northern rim of the La Fossa cone (De Fiore 1922). Subsequent episodes of increased fumarolic gas discharge, temperatures, and exhaling surface areas occurred in 1978, 1987–1993 (when the fumarolic area reached temperatures up to 690 °C), 1996–1998, 2004/2005, and 2021–2023

Editorial responsibility: L. Pioli

✉ Silvia Giansante
silvia.giansante@ingv.it

1 Istituto Nazionale Di Geofisica E Vulcanologia, Sezione di Pisa, Via Cesare Battisti 53, 56125 Pisa, Italy

2 Department of Earth Sciences, University of Florence, Via La Pira 4, 50121 Firenze, Italy

3 Department of Earth Sciences, University of Pisa, Via S. Maria 53, 56126 Pisa, Italy

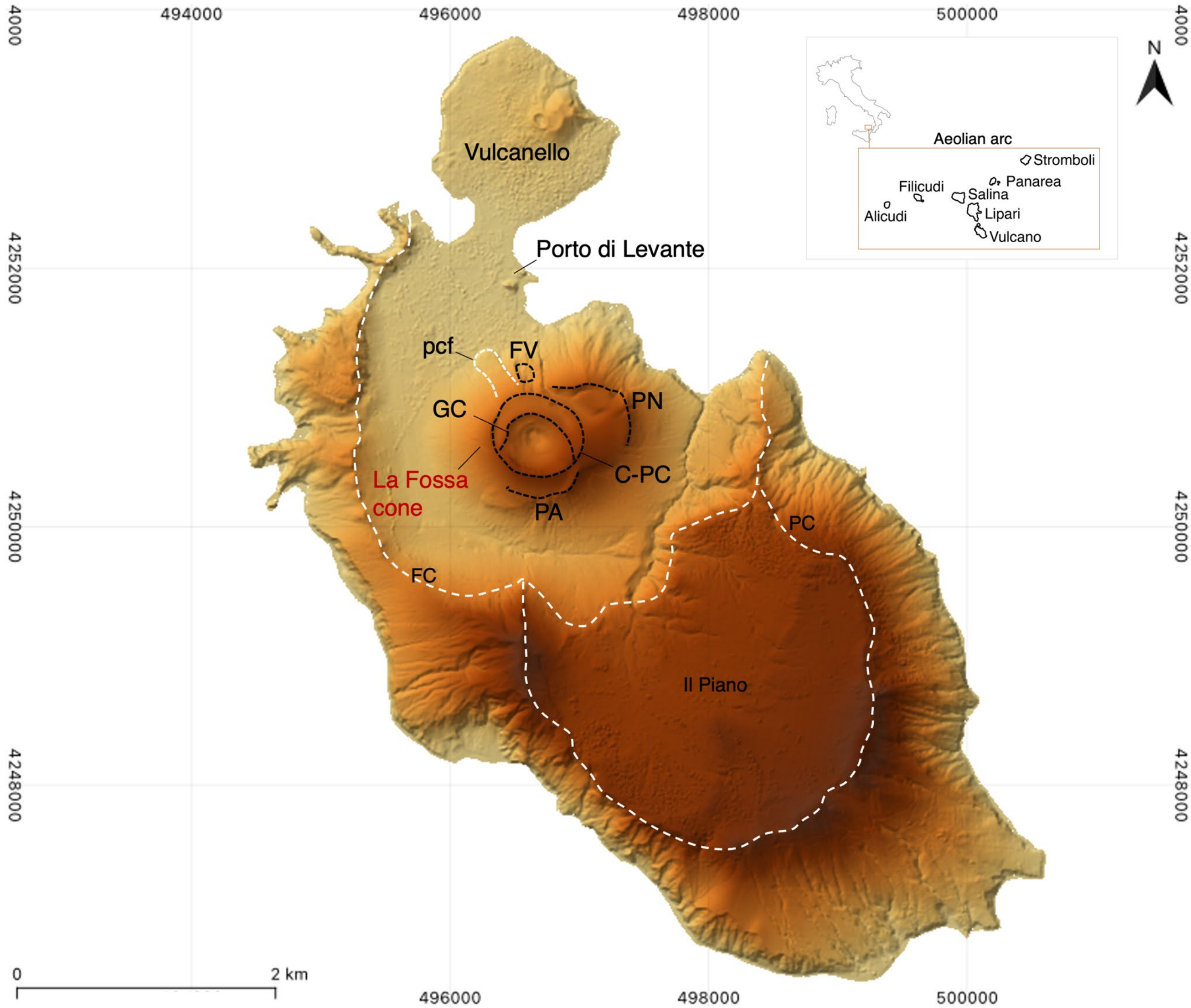

Fig. 1 Map of Vulcano Island within the Aeolian Arc, Italy: *PN*, Punte Nere crater; *PA*, Palizzi crater; *FV*, Forgia Vecchia craters; *C-PC*, Commenda and Pietre Cotte craters; *pcf*, Pietre Cotte lava flow; *GC*, Gran Cratere crater; *PC*, il Piano Caldera; *FC*, La Fossa Caldera (Frazzetta et al. 1983; De Astis et al. 2013)

(Barberi et al. 1991; Chiodini et al. 1995; Harris et al. 2012; Capasso et al. 2014; Federico et al. 2023).

The recent unrest (2021–2023), attributed to increased heat and gas fluxes from a deeper magmatic source (Aiuppa et al. 2022; Inguaggiato et al. 2022; Di Traglia et al. 2023; Federico et al. 2023), heightened the scientific interest in potential phreatic eruptions on the island, especially with the growing popularity of Vulcano as a tourist destination. The population varies in fact from 800 during winter to peaks of 22,000–28,000 visitors in July and August (Bonadonna et al. 2021), raising risk even in the case of small-scale eruptions.

Historical and stratigraphic records at Vulcano have provided evidence of at least three significant phreatic events (> 10^4 m^3) in the past 1000 years (Frazzetta et al. 1983; Gurioli et al. 2012; Rosi et al. 2018; Selva et al. 2020). Between 1873 and 1888, La Fossa volcano experienced small-scale explosive activity, including low-magnitude phreatic events, according to historical descriptions of explosion dynamics and ejected products (Mercalli 1886; Mercalli and Silvestri 1891), as well as stratigraphic evidence (this work; Di Traglia et al. 2024).

We present a compilation of historical information on the 1873–1888 explosive activity and describe the 1873 phreatic deposit based on field surveys and laboratory data. We then use a physical model and three-dimensional multiphase flow simulations to consider explosion dynamics. Comparing historical accounts, volcanological data, and simulation results, we discuss the eruption dynamics and associated hazard.

Geological background and last 1000 years of activity at La Fossa

Vulcano Island formed from the progressive coalescence of diverse volcanic structures over approximately 120 ky (Keller 1980; Frazzetta et al. 1983; De Astis et al. 2013). The La Fossa composite cone (391 m asl), along with Vulcanello, is the most recent volcanic centre, rising in the middle of its namesake caldera. Over the past 5.5 ky, La Fossa has experienced multiple eruptive cycles producing explosive (phreatomagmatic/phreatic, Vulcanian, Strombolian, Sub-Plinian) and effusive activity from different craters (Fig. 1; Keller 1980; Frazzetta et al. 1983, 1984; De Astis et al. 2013; Di Traglia et al. 2013, 2024; Selva et al. 2020). To avoid ambiguity, we adopt the term *phreatic* to denote shallow explosive events driven by the expansion of steam and/or gas related to increased heat and gas fluxes from magma stored in a relatively deep reservoir (Mastin 1995; Browne and Lawless 2001). Erupted products range from latites to rhyolites, with minor shoshonites (Keller 1980; Frazzetta et al. 1983; Gioncada et al. 2003; Boyce et al. 2007; De Astis et al. 2013; Costa et al. 2020).

La Fossa has been particularly active in the last 1000 years (Fig. 2a). Di Traglia et al. (2013) initially divided this period into two main Eruptive Clusters: the Palizzi-Commenda (XII–XIII century) and the Gran Cratere (fifteenth century–1890 CE). Later, Di Traglia et al. (2024) refined this into the Palizzi, Commenda, Fossa-Forgia Vecchia, Pietre Cotte, and Gran Cratere eruptive units, separated by seven erosive unconformities.

The Palizzi unit, starting in ~900 CE from summit vents (Di Traglia et al. 2024), involved four main explosive and two effusive phases, the latter producing the Commenda rhyolitic lava and the Punte Nere, Campo Sportivo, and Palizzi trachytic lava flows (Gurioli et al. 2012; Di Traglia et al. 2013, 2024; Rosi et al. 2018).

The Commenda unit comprises the lithic-rich Breccia di Commenda deposit (1240–1300 CE; Gurioli et al. 2012; Rosi et al. 2018; Di Traglia et al. 2024) emplaced as pyroclastic density currents (PDCs) and minor fallout activity, followed by a long-lasting ash fall depositing a thinly stratified, reddish ash sequence ("Tufi Varicolori"; Frazzetta et al. 1983; Capaccioni and Coniglio 1995; Dellino et al. 2011; Rosi et al. 2018) that resulted in building part of the La Fossa cone. The Breccia di Commenda event represents the largest ($> 2 \times 10^6$ m^3) phreatic eruption recorded on Vulcano Island (Gurioli et al. 2012; Rosi et al. 2018).

The Fossa-Forgia Vecchia unit (fifteenth to sixteenth centuries) records alternating phreatic and magmatic events from La Fossa, including the phreatic deposits expelled from two lateral vents: Forgia 1 (1444 CE) and Forgia 2 (1444–1550 CE). This activity was followed by the Pietre Cotte pyroclastic units and the overlying Pietre Cotte rhyolitic lava flow (1631–1786 CE; Di Traglia et al. 2024).

The uppermost sequence of the Gran Cratere unit was emplaced after 1786 CE (Di Traglia et al. 2024). It includes phreatic breccia deposits emplaced between 1873, which form the subject of this paper, and early August 1888 (Fig. 2a; GCa in Di Traglia et al. 2024), as well as the subsequent magmatic Vulcanian eruption of 1888–1890 (GCb in Di Traglia et al. 2024).

Since 1890, La Fossa has been characterised by continuous fumarole and soil degassing (Selva et al. 2020; Inguaggiato et al. 2022; Aiuppa et al. 2022; Federico et al. 2023).

The 1873–1888 activity from contemporary chronicles

The La Fossa crater has been industrially exploited since at least 1800 for the extraction of sulphur and alum and the production of boric acid. Possibly also for these reasons, crater changes or activity has been often described in detail by local observers.

A few years before 1873, La Fossa was characterised only by mild fumarolic degassing (Salino 1874; Mercalli 1883; Mercalli and Silvestri 1891; De Fiore 1922). In July 1873, approximately 2 months before the beginning of the eruption, workers within the La Fossa crater witnessed intensified outgassing and uncommon hiss from fumarolic vents (Salino 1874). An enlargement of the exhaling area was also observed (De Fiore 1922). This activity escalated into a series of phreatic events impacting the flanks of the cone, occurring in four main phases: 1873, 1878/1879, 1886, and the opening phase (3–5 August) of the 1888–1890 eruption (Fig. 2b). Mercalli (1886) and Mercalli and Silvestri (1891) described the material ejected in these phases as consisting of non-juvenile, variably altered fragments.

The September–October 1873 activity was directly observed by Ambrogio Picone, mining director on the island between 1873 and 1876; his descriptions (see Supplementary Table 1) depicted the 1873 activity as impulsive, marked by repeated short events of varying intensity (Fig. 2c; Salino 1874; Mercalli and Silvestri 1891; De Fiore 1922). Conspicuous fumarolic activity preceded each explosion and, a few minutes before each explosion, loud noises were heard from the crater, accompanied by changes in fumarolic emissions. Single explosions lasted for 10 to 15 min and occurred at intervals of 20 to 30 min. These events ranged from simple ash emission to explosions ejecting also blocks (Supplementary Table 1; De Fiore 1922). Larger ejecta were projected up to 800 m above the eruptive vent, with most landing near

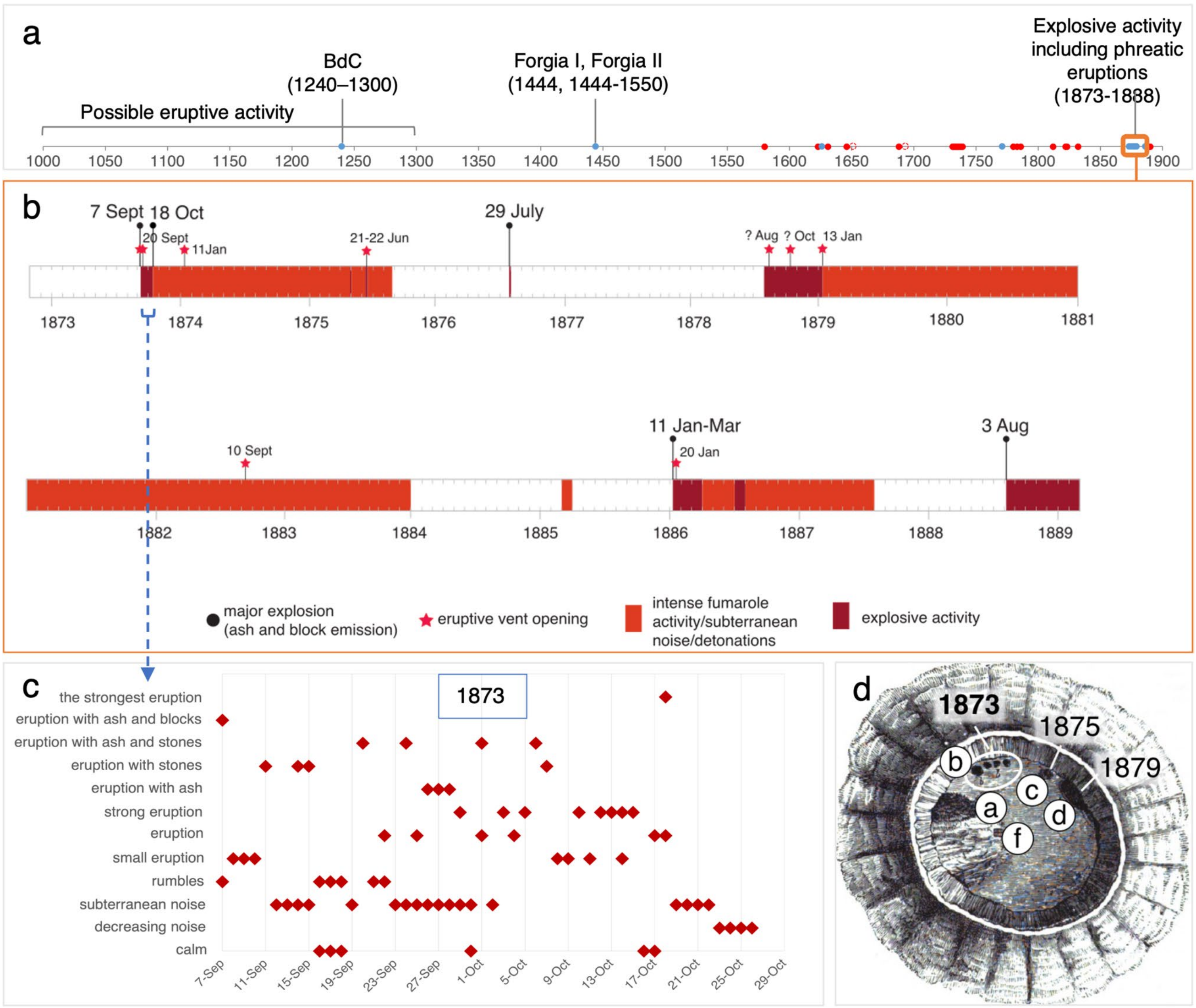

Fig. 2 **a** Eruptive activity at La Fossa in the 1000–1900 CE period. Dashed circles represent uncertain events (De Fiore 1922) while blue dots indicate the Breccia di Commenda (BdC, 1240–1300), Forgia I (1444), Forgia II (1444–1550), and 1873–1888 phreatic events (Mercalli and Silvestri 1891; De Fiore 1922); **b** activity observed at La Fossa between September 1873 and February 1889 (Mercalli 1883; Mercalli and Silvestri 1891; De Fiore 1922); **c** detail of the 1873 activity (Salino 1874; Mercalli 1883; Mercalli and Silvestri 1891; De Fiore 1922); **d** La Fossa crater morphology shortly after the January 1879 eruption: *a*, large fumaroles active in October 1878; *b*, four vents opened between September and October 1873, with the two extremes reactivated in 1879; *c*, vent opened in 1875, enlarged in September 1877, and inactive in 1879; *d*, large vent opened during the night of 10/11 January 1879; *f*, factory. Modified after Mercalli (1883)

the La Fossa crater rim and on the northern flank, while only a few settled within the crater. Over the 44-day-long activity, at least nine explosions ejecting blocks occurred at intervals ranging from 1 day to more than a week. In many cases, historical chronicles do not specify if ash or coarser material was ejected (Fig. 2c, Supplementary Table 1).

Ground inflation and deflation were also directly observed during the explosions (De Fiore 1922), while no obvious seismic activity was described preceding or accompanying the explosive events. Despite not causing damage to the inhabited area of Vulcano Porto, ash covered the island for days before being completely remobilised by rainfall and winds. Occasionally, prevailing winds carried the ash to the neighbouring islands of Salina and Lipari (Salino 1874; De Fiore 1922).

Between 1873 and 1879, at least six eruptive vents opened within the La Fossa crater, with four of them excavated during the 1873 event (Fig. 2d; Mercalli 1883; Mercalli and Silvestri 1891; De Fiore 1922).

Materials and methods

Fieldwork focused on identifying and describing the stratigraphic, sedimentological, and physical features of the 1873 phreatic deposit emplaced in the north-western flank of the La Fossa cone, with additional investigations on the southern slopes. Stratigraphic logs were compiled at each site, correlating stratigraphy and collecting samples from the main units at the most complete outcrops.

Samples were mechanically dry-sieved at half-phi intervals ($\phi = -\log_2(d/d_0)$, where d is the particle diameter in millimetres and $d_0 = 1$ mm) for the fraction ≥ 250 µm. The fraction below 250 µm was analysed using a Malvern Morphologi G3 static particle analyser. Grain-size distributions were obtained by combining data from both techniques, assuming constant density across different classes. Abundances of particles with diameters of 355 and 250 µm, as identified by the particle analyser, were combined with the size bin immediately below (i.e. 177–255 µm).

Isopach maps were compiled for the different stratigraphic units. Given the complex isopach shapes and highly variable thickness of the deposit that does not thin out regularly with distance, we estimated the volume of the deposit using the trapezoidal rule (Froggatt 1982; Fierstein and Nathenson 1992). This method avoids thickness extrapolation with distance implied in other methods and only uses isopachs based on observed thickness data. The uncertain eruptive vent location and unknown deposit distribution in the proximity of the source (tens of meters) complicated isopach contour tracing. Consequently, our calculations might underestimate thickness in very proximal areas. Volume determination considers two different extensions of the zero isopach: one based on measured data and another assuming a larger affected area up to approximately 1 km from the La Fossa north-western crater rim.

To model the dispersal of the ejected products, the pre-1888 morphology of the La Fossa crater and cone were reconstructed from the 1868 topographic map of Vulcano Island. The historical map, obtained from the Italian Istituto Geografico Militare (IGM), was geo-referenced using a recent digital elevation model (DEM; 1 m of resolution) of the island as a reference, aligning areas with similar morphology. Contour lines were digitised at 5-m intervals for the La Fossa crater and 10 m for the cone flanks, approximating the vertical accuracy of the map. The QGIS open-source software was used to extract contour lines and generate two interpolated DEMs with a 1-m-spaced grid, which were then merged with a 2-m grid using an appositely written Python script to minimise altitude differences in overlapping zones.

Geological and field-derived data were used to infer input parameters for physical modelling (see the "Initial conditions for simulations" section). The numerical study uses the new transient, three-dimensional, multiphase flow model OpenPDAC (de' Michieli Vitturi, 2024; see Supplementary Information), an OpenFOAM module based on the equations of the PDAC model (Neri et al. 2003; Esposti Ongaro et al. 2012). OpenPDAC describes the explosion dynamics of a gas and fine particle mixture (Eulerian description) one-way coupled with coarser ballistic particles (Lagrangian model; de' Michieli Vitturi et al. 2010). The model assumes that an eruption is triggered by the sudden decompression of high-temperature, high-pressure fluids (water) and fragmented rocks, resulting in a multiphase mixture ejected into the atmosphere. The effect of the flashing of these fluids is not taken into account as water is considered already in vapour state.

The "Breccia De Fiore" deposit

Stratigraphy

A complex stratified breccia and tuff deposit, rich in hydrothermally altered clasts, was found in the north-western flank of the La Fossa cone (Fig. 3a). This deposit, named here Breccia De Fiore (BDF) after Prof. Ottorino De Fiore, who extensively documented the activity of La Fossa in the 1873–1888 period, is interbedded between the deposits of the Pietre Cotte eruptive sequence and the products of the last magmatic eruption of 1888–1890 (Fig. 3b).

Based on eyewitness accounts reporting vent opening in the northern sector of the La Fossa crater (Mercalli 1883), the duration of the activity (a total of 44 days), and field observations, we confidently attribute the BDF to the 1873 eruptive phase, the most intense phreatic crisis between 1873 and early August 1888. Because of their stratigraphic features, further phreatic deposits below the 1888–1890 Vulcanian phase cropping out in the south-eastern flank and south-western crater rim (Fig. 3a) were not correlated with those in the western and north-western side, and they were considered associated to younger eruptive episodes.

The BDF is a very poorly sorted lapilli tuff or tuff breccia, with centimetric to pluri-decimetric thickness (45 cm on average), composed of fragments ranging from fine ash to coarse lapilli and minor blocks. Throughout its whole thickness, the deposit comprises heterogeneous, variably hydrothermally altered clasts. While less common, a fraction of clasts exhibits significant surface alteration, manifesting as white, yellow, or red colour, that obscures their original lithology (Supplementary Figure 1). Conversely, many clasts are either unaltered or show only partial surface alteration, allowing their original lithology to be identified. These clasts mainly include dense fragments of trachyte, rhyolitic obsidian, and flow-banded rhyolite lava flows, alongside smaller

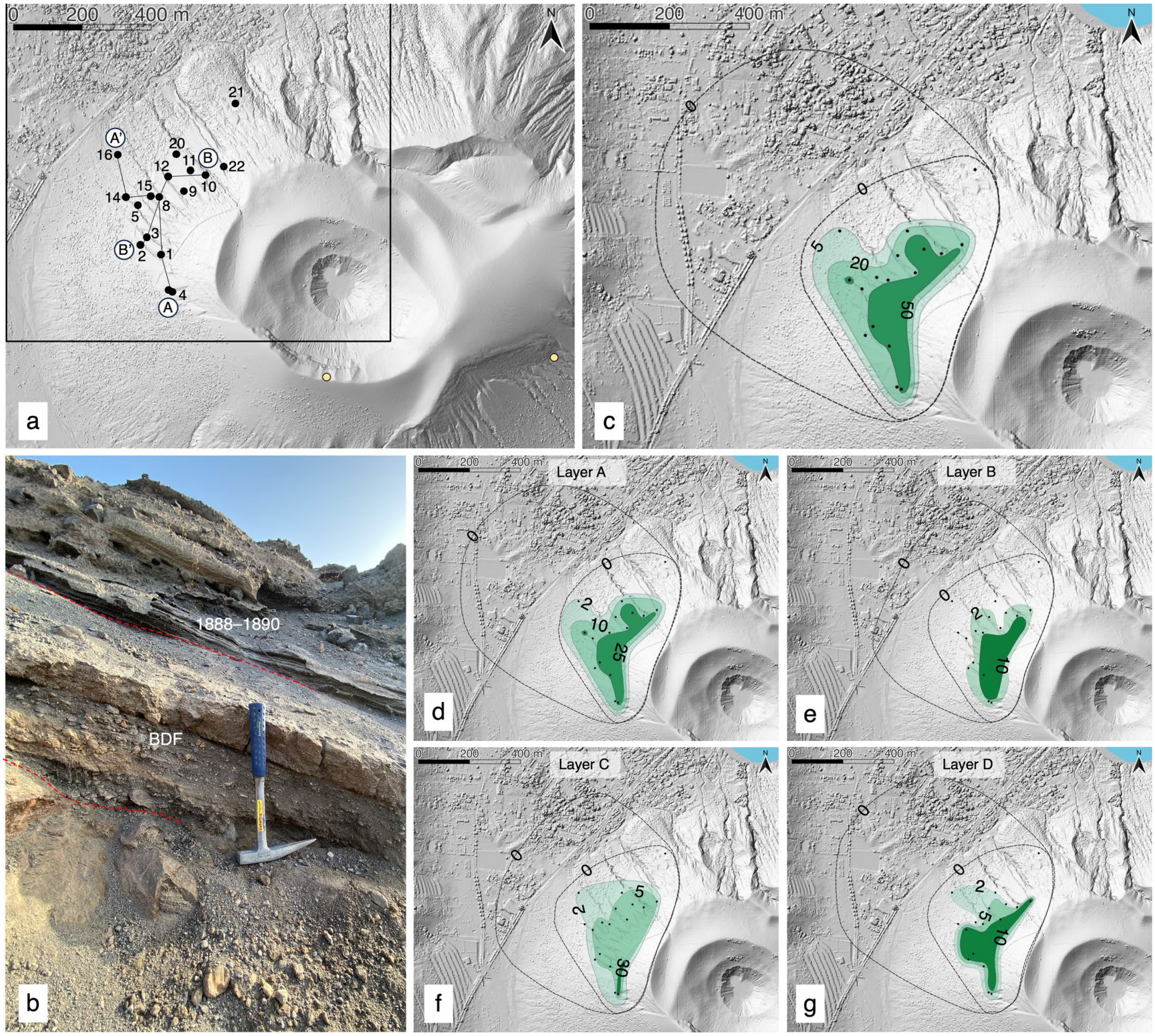

Fig. 3 **a** Map showing the location of the BDF sections (black dots) and additional phreatic breccia deposits (yellow dots) beneath the 1888–1890 Vulcanian phase. Traces of key sections are marked along (A-A') and across (B-B') the deposit; **b** field view of the BDF stratigraphic position. Isopach maps (in cm) for the whole BDF sequence (**c**), layer A (**d**), layer B (**e**), layer C (**f**), and layer D (**g**) are also shown, including two different extensions of the 0-isopach

amounts of vesicular clasts, such as pumice, scoria, and tuffs (Supplementary Figure 1). These clast types are identified throughout the BDF sequence and closely resemble the material from the eruptions of 1879, 1886, and 3–5 August 1888 (Mercalli 1886; Mercalli and Silvestri 1891). Notably, macroscopic observations on the alteration state of the clasts often do not reflect microscopic findings, suggesting that surface alteration alone cannot be considered a reliable indicator of the type and extent of hydrothermal alteration affecting the BDF material. The general absence of a homogeneous population of glassy, unaltered clasts representative of a juvenile component, as well as the abundance of hydrothermally altered clasts, is considered evidence of the phreatic origin of the deposits.

Despite its complexity, the BDF exhibits distinguishable characteristics, such as sedimentological, grain size, and colour variations, allowing the identification of five layers generally separated by planar surfaces, denoted as layer A to layer E. These layers can be recognised and laterally correlated throughout the main stratigraphic sections (Fig. 4).

Layer A (3–30 cm) is a grey, matrix-supported, fine lapilli-bearing layer at the base of the BDF sequence (Figs. 4 and 5). It is usually above an erosive surface and cuts into a brownish ash deposit at the top of the Pietre Cotte cycle or

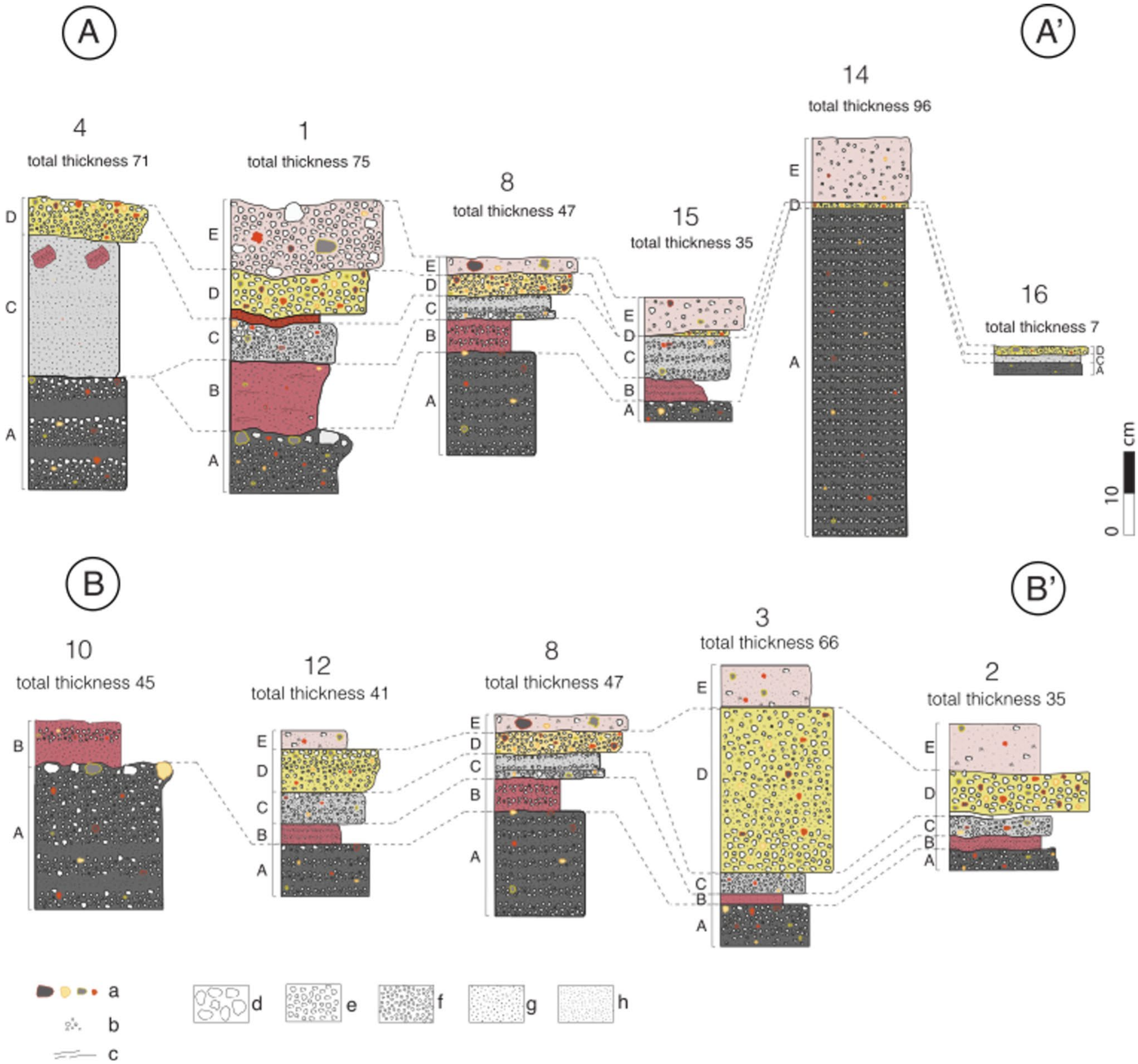

Fig. 4 Stratigraphic correlations among the different sections of the BDF along A–A' and B–B' profiles; *a* Altered clasts; *b* vesiculated matrix; *c* weak lamination; *d* blocks; *e* coarse lapilli; *f* fine lapilli; *g* coarse ash; *h* fine ash. Maximum thickness values are shown for each layer

into reworked deposits related to lahars or slope grain flows. The ash content ranges between 35 and 90 wt.%, with the highest values corresponding to the more lateral and distal outcrops (Supplementary Table 2). The deposit varies from massive, reversely graded, poorly sorted (e.g. Sections 1, 3, 15; Figs. 4 and 5a, e) to stratified, with alternations of well-sorted, reversely graded, fine lapilli beds and coarse to fine ash beds (Fig. 5b, g). In its uppermost portion, it is often characterised by a concentration of coarse lapilli (2–5 cm in diameter) and minor blocks with an average diameter of 11–15 cm (Fig. 5a, f). Layer A coarsens at Sect. 10, where a laterally discontinuous, openwork-textured bed of blocks and coarse lapilli is present at the top (Figs. 4 and 5d). In drainage channels close to the base of the cone (i.e. Section 14), this layer is thickened by reworked material forming alternations of parallel-bedded ash and lapilli layers (Figs. 4 and 5c). At the most distal sector, layer A grades into a weakly laminated, thin level of grey to yellowish, coarse ash (Figs. 4 and 5h).

Layer B (1–18 cm) is an ash-rich, matrix-supported, laminated to stratified reddish to brownish bed (Supplementary Table 2). It is formed by an alternation of well-sorted, fine to coarse ash up to fine lapilli beds (e.g. Sections 8, 10 in Figs. 4 and 5b). Locally, layer B shows weak laminations

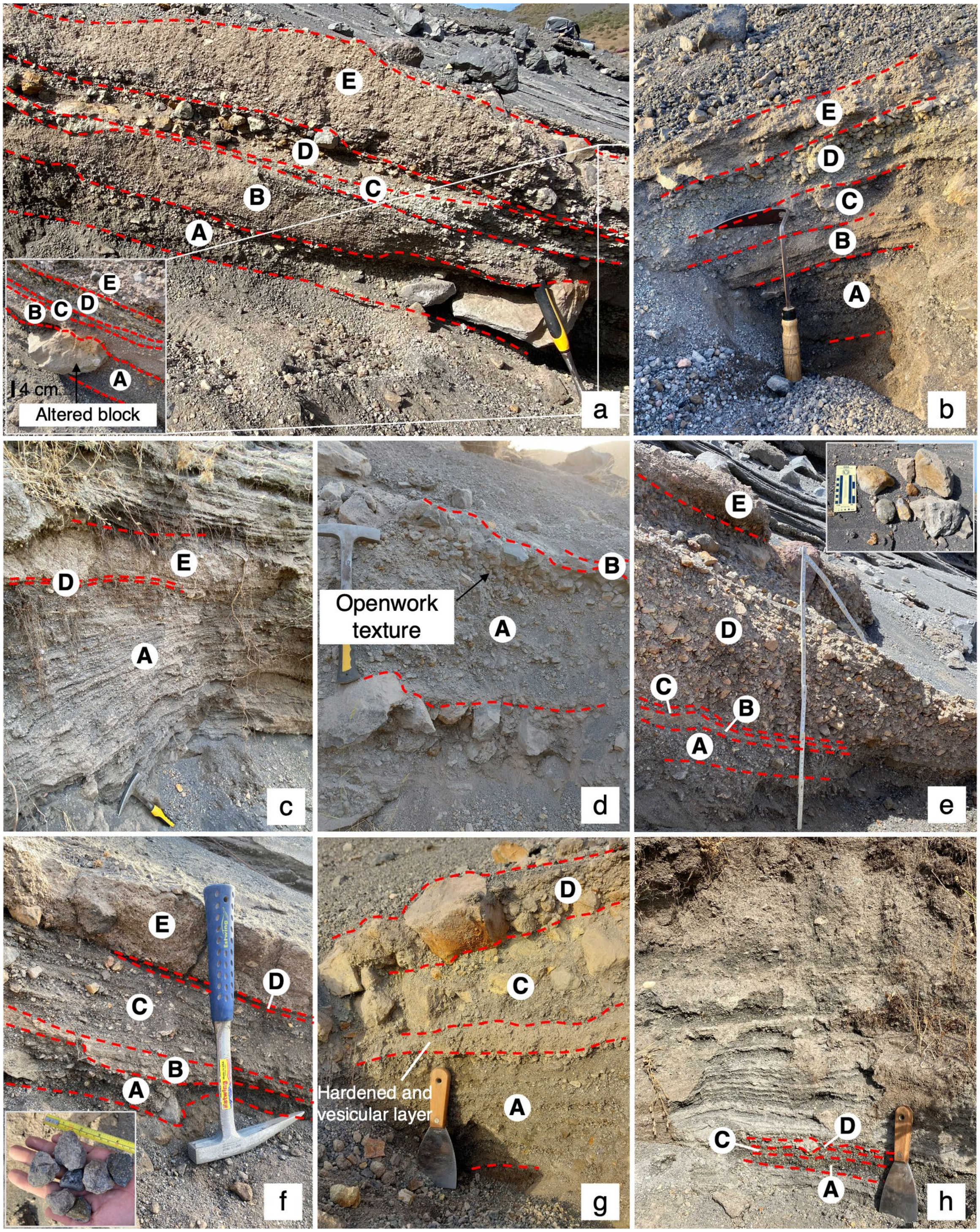

Fig. 5 Image showing the BDF deposit at Sects. 1 (**a**), 12 (**b**), 14 (**c**), 10 (**d**), 3 (**e**), 15 (**f**), 9 (**g**), and 16 (**h**). Coarse lapilli from the top of layer A are also shown for Sects. 3 (**e**) and 15 (**f**)

and reverse grading (Fig. 5a, e, f). It is absent in the most lateral sections (i.e. Sections 4 and 9) and at the base of the cone (i.e. Sections 5, 14, and 16; see Figs. 4 and 5c, g, h).

Layer C (2–35 cm) is a grey, matrix-supported, and fine-to-coarse lapilli-bearing deposit (Supplementary Table 2), with an internal structure varying from massive to stratified (Fig. 5g, f). In most cases, stratification includes alternating levels of fine-to-coarse ash and fine-to-coarse lapilli. Coarse, lapilli-bearing lenses (e.g. Section 1) and scattered clasts of 5–10 cm in diameter are locally present (Fig. 5f, g). At the foot of the north-western flank of the cone, this layer is represented by a 2-cm-thick massive bed of fine to coarse ash (Figs. 4 and 5h). Layer C is absent in the easternmost outcrops (i.e. Sections 10, 11).

Layer D (1–39 cm) is the most characteristic and coarsest bed of the sequence (Supplementary Table 2). It is a yellow, clast- to locally matrix-supported layer composed of moderately-to-well-sorted, fine-to-coarse lapilli and scattered blocks. The layer is absent only at Sect. 10 (Figs. 4 and 5d), possibly removed by erosion. It is generally massive, with the exception of Sect. 3 where it is organised in a clast-supported basal portion of moderately sorted, coarse lapilli, a central portion of fine-to-coarse lapilli with abundant ash, and a clast-supported, poorly sorted top portion composed of coarse-to-fine lapilli (Fig. 5e). It can also show reverse grading (Fig. 5b, e).

Layer E (3–18 cm) caps the whole BDF eruptive sequence in almost all outcrops (Figs. 4 and 5). It is a hardened, massive, matrix-supported, grey to pinkish layer composed of fine-to-coarse lapilli and rare blocks set in a vesicular, fine, cohesive ash matrix. The matrix content tends to increase moving down to the base of the cone. Vesicles are mostly concentrated in the matrix at the base of the layer.

Unlike layers A, B, C, and D, which are thicker in the north-western sector of the cone and can show lateral thinning at the scale of the outcrop (Fig. 5), the thickness of layer E is higher in proximal (i.e. Sections 1, 3, 12) and distal (i.e. Sections 14 and 15) zones compared to the central outcrops (see Sects. 5 and 8 in Fig. 4).

Sample grain-size and total grain-size distribution (TGSD)

Samples from eight sections (i.e. 1, 2, 3, 4, 10, 14, 15, 16) located in the different sectors of the BDF deposit were selected to investigate grain-size variations (Supplementary Table 2). Samples generally show multi-modal grain-size distributions that can be deconvoluted in two to four normal subpopulations (SP-A to SP-D) of variable weight in each sample (Supplementary Table 3). Their mean values cluster into four groups for which average mean (μ) and sorting (σ) values can be defined: SP-A, $\mu = -3.7$ φ and $\sigma = 0.7$; SP-B, $\mu = -1.6$ φ and $\sigma = 1.1$; SP-C, $\mu = 0.9$ φ and $\sigma = 0.14$; SP-D, $\mu = 5.5$ φ and $\sigma = 1.0$.

The coarsest layers are generally A and D, often presenting a pronounced mode (up to 25–50 wt.%) in the coarse lapilli fraction. Grain-size distributions of layers C and E are enriched in fine-to-medium lapilli (up to 44 wt.%) with Mdϕ − 1.43–0.38 and − 1.4, respectively (Supplementary Table 2). Layer B represents the finest-grained bed, with 82–86 wt.% of coarse-to-fine ash (Supplementary Table 2).

In terms of SPs, the coarsest SP-A is never present in layer B samples, the latter being dominated by SP-C (around 70 wt.% of the total). Contribution of SP-A is instead important only for A and D layers (on average 20 wt.% and 35 wt.%, respectively, for all the samples, except for the most distal ones), while values generally lower than 17 wt.% characterise layers C and E. The finer-grained SP-D is always present in all the layers, although in a very low amount (generally below 5 wt.%).

Given the good areal coverage of the analysed samples, grain-size data from all the stratigraphic sections and layers were weighted by the relative thickness of each layer to estimate a total grain-size distribution (TGSD) for the whole deposit. TGSD was estimated both directly averaging weighted grain-size distributions of each sample and the relative weight of the four normal subpopulations listed above in each sample. The resulting TGSD is markedly bimodal, with peaks at ~ − 4 and 1 ϕ and a negligible contribution of fine ash (Fig. 6).

Isopach maps and volume estimation

Figure 3c displays the isopach map for the total BDF deposit, obtained from the integration of thickness data. The absence of the deposit along the most proximal slopes of the cone is possibly due to non-deposition, as well as to the intense post-eruption erosion of the pyroclastic cover in this sector of the volcano (Ferrucci et al. 2005). The deposit is characterised by a total thickness of 50 cm at about 130 m from the north-western crater rim. Thickness decreases to 5 cm at the base of the cone, about 400 m from the north-western crater rim. Isopach maps for layers A, B, C, and D are shown in Fig. 3d–g.

Based on isopach maps, we estimated the volume of the total BDF deposit at 3.7– 4.6×10^4 m^3 (Table 1). The volume of individual layers varied between 6.4×10^3 and 1.9×10^4 m^3 (Table 1), with layer A representing the most dispersed and voluminous. These values have an uncertainty of up to 80% based on the extent of the zero isopach used in the calculations (Table 1).

Assuming a deposit density of 1300 kg/m^3 and a porosity of 35–40%, we estimated an erupted mass in the range of 3.0–4.0×10^7 kg for the whole BDF deposit, with a maximum value of 5.0×10^7 kg considering potential losses. For individual layers of the sequence, the erupted mass estimates under the same assumptions ranged from 5.0×10^6 to 1.5×10^7 kg, with a maximum value of 2.0×10^7 kg with potential losses included. These estimates could underestimate the deposit volume, as they may not encompass (i) fine-grained distal material that could have been dispersed by convection/diffusion (the low relative weight of the fine-grained SP4 in the TGSD however suggests a limited effect of this process); (ii) the material that might have been lost due to syn- and post-eruption processes of remobilisation, erosion, and elutriation of fine particles (the latter however

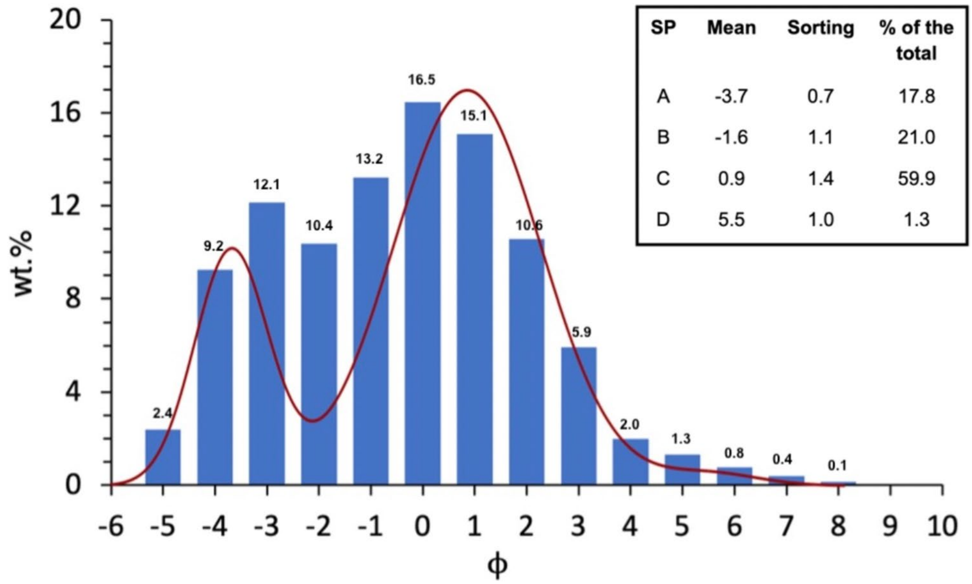

Fig. 6 TGSD (wt.%-diameter in ϕ-scale) of the BDF reconstructed from the weighted sum of the grain size distribution of each sample. The red line shows the TGDS as resulting from weighting the contribution to each sample of the different normal subpopulations SP-A to SP-D

not clearly described in the chronicles); and (iii) the material resedimented inside the La Fossa crater and not found in the deposits observed on the flanks of the cone (at least 20%).

Physical and numerical modelling

Our numerical modelling is aimed at reconstructing eruption dynamics and evaluating the influence of initial parameters on the behaviour of the eruptive mixture and product distribution, for comparison with field observations of deposit dispersal and eruption timing.

Based on field observations and historical chronicles (see the "Discussion" section), we assumed a scenario involving gas accumulation and overpressure build-up at shallow depths beneath the La Fossa crater, exceeding the tensile strength of rocks (Browne and Lawless 2001; Stix and De Moor 2018), followed by explosive decompression of a mixture of gas and fragmented material in the atmosphere.

Table 1 Volume estimates for the total BDF and for layers A, B, C, and D

	Case[a]	Volume (m^3)
Total BDF deposit	1	3.66×10^4
Total BDF deposit	2	4.59×10^4
Layer A	1	1.57×10^4
Layer A	2	1.94×10^4
Layer B	1	6.37×10^3
Layer B	2	8.52×10^3
Layer C	1	1.24×10^4
Layer C	2	1.48×10^4
Layer D	1	6.46×10^3
Layer D	2	1.01×10^4

[a]Cases 1 and 2 represent volume calculations considering a smaller (1) and a larger (2) 0-isopach contour

Initial conditions for simulations

Each eruptive scenario was defined by specifying the geometric boundary conditions (eruptive vent and volcano morphology) and key eruption parameters, such as the ejected solid mass, initial pressure and temperature of the water vapour and ash material, and gas volume fraction. Additionally, the physical properties of the eruptive mixture were defined, including gas composition, particle size, and density.

The input parameters for these scenarios, summarised in Table 2, were constrained using field and geological data. Pre-eruption topography, vent position and geometry were based on available historical data and field evidence. The 1888–1890 eruption significantly modified the La Fossa cone topography and the crater area (Supplementary Fig. 2), which was filled by approximately one-third (Mercalli and Silvestri 1891; De Fiore 1922). To simulate an eruption in a topographic setting like that before 1888, we used a reconstructed DEM from the digitisation of the 1868 contour line map of Vulcano Island (see the "Materials and Methods" section). Given the absence of any residual structure related to the phreatic vents formed in 1873 and according to the descriptions of Mercalli (1883), we positioned the explosion vent inside the Gran Cratere crater of La Fossa, near the northern wall. This vent was modelled as a prolate hemispheroid shape with a specific radius (semi-minor axis) and depth (semi-major axis). Historical descriptions (Mercalli 1883) suggest the explosion vents possibly measured up to 20 m in diameter. However, to accommodate

Table 2 Input parameters of numerical modelling. *ID*, simulation identifier; *R/D*, vent radius and diameter; *V*, *M*, ejected volume and ejected mass of particles; α_p, ash particle volume fraction within the eruptive vent; *P*, *T*, initial pressure and temperature of the gas-ash mixture in the vent; d_p, ash particle diameter; *E*, E_m, total explosive energy and specific energy (considering a bulk density of 600 kg/m^3)

ID	*R/D*	*i, d*	*V* (m^3)	*M* (kg)	α_p	*P* (MPa)	*T* (°C)	d_p (mm)	*E* ($\times 10^{11}$ J)	E_m (kJ/kg)
1	20/100	0°	2.5×10^4	5×10^7	0.3	5	250	1	5.8	12
2	20/100	21°, W	2.5×10^4	5×10^7	0.3	5	250	1	5.8	12
3	20/100	21°, NW	2.5×10^4	5×10^7	0.3	5	250	1	5.8	12
4	15/150	21°, W	2.1×10^4	4.2×10^7	0.3	5	250	1	5.8	12
5	20/100	21°, W	2.5×10^4	5×10^7	0.3	7	250	1	8.5	17
6	20/100	21°, W	2.5×10^4	5×10^7	0.3	3	250	1	3.2	6
7	20/100	21°, W	5×10^4	1×10^8	0.6	5	250	1	3.3	3
8	20/100	21°, W	2.5×10^4	5×10^7	0.3	5	400	1	5.8	12
9	20/100	21°, W	2.5×10^4	5×10^7	0.3	5	250	0.177	5.8	12
10	10/100	0°	6.3×10^3	1.3×10^7	0.3	5	250	1	1.5	12
11	10/100	21°, W	6.2×10^3	1.2×10^7	0.3	5	250	1	1.5	12
12	10/100	21°, NW	6.3×10^3	1.3×10^7	0.3	5	250	1	1.5	12
13	10/100	21°, W	1.3×10^4	2.5×10^7	0.6	5	250	1	0.83	3

a predetermined volume of particle and gas, we assumed vent diameters ranging from 20 to 40 m, with depths of 100 to 150 m (Table 2). In some scenarios, the geometry of the source area was inclined at a 21° angle (Table 2) with respect to the vertical axis by translating horizontally the base of the hemispheroid.

The magnitude of eruption scenarios was constrained based on estimates of the total erupted mass. As outlined in the "Isopach maps and volume estimation" section, these estimates were derived from the deposit volumes of both the total BDF sequence and its individual layers (Table 1). Accordingly, the modelled scenarios encompass magnitudes ranging from 1.0×10^7 to 5.0×10^7 kg, with an upper limit of 1.0×10^8 kg (Table 2).

The initial temperature of the gas-particle mixture was set at 250 °C as the minimum value, based on stable mean values recorded at the fumaroles at the summit of La Fossa before the 2021 unrest (Diliberto 2021). Although higher values cannot be excluded, we considered a maximum initial value of 400 °C, in the range of the peak temperature registered throughout the 2021–2023 crisis (Federico et al. 2023).

We assumed homogeneous pressure within the eruptive vent, exploring a range of 3–7 MPa (Table 2) based on lithostatic pressure and rock fragmentation thresholds. At a depth of 100 to 150 m below the La Fossa crater, the lithostatic pressure ranges between 1.9 and 2.9 MPa (considering an average rock density of 2000 kg/m^3). The initial pressure in the vent must be higher than these values. Typical fragmentation thresholds (Spieler et al. 2004; Scheu et al. 2006; Koyaguchi et al. 2008; Mayer et al. 2016) are between 2 and 5 MPa (e.g. Mayer et al. 2015, 2016; Montanaro et al. 2016). Because we do not model fragmentation and the energy spent in fragmentation is typically in the order of 10–15% of the total energy (Montanaro et al. 2016), we assumed that the initial overpressure is of the same order of magnitude of the rock fragmentation threshold.

The total explosive energy (E), expressed in Joules, was calculated using an ideal gas model, considering the adiabatic and reversible expansion of water vapour (Montanaro et al. 2016):

$$E = \left[\frac{P_0 \times V_{wv}}{\gamma - 1}\right] \times \left[1 - \left(\frac{P_{atm}}{P_0}\right)^{\frac{\gamma-1}{\gamma}}\right]$$

where P_0 represents the initial pressure (Pa) within the vent prior to the explosion, V_{wv} is the initial volume of water vapour (m^3) in the vent, P_{atm} is the atmospheric pressure (Pa), and γ is the ratio of specific heats (i.e. about 1.3 for water vapour). From the average density per unit volume (J/m^3), the initial particle volume fraction, and fine particles average density (2000 kg/m^3), we calculated the average specific energy (energy per unit of mass) available in the explosion in the range of 3–17 J/kg (Table 2).

The initial porosity of the host rocks determines the volume fraction of gas in the explosion vent; thus, it defines the specific energy available in the explosion (Montanaro et al. 2016). To account for this factor, we set a fixed volume fraction of gas, and consequently of ash, within the eruptive vent. However, the initial gas volume fraction does not directly correlate with the actual initial porosity of source rocks, as it represents, in our simulations, the amount of gas and hence the energy available for expansion after fragmentation and just before the initial expansion (fragmentation energy is not considered in the calculation). As initial conditions, we either assumed a porosity of 40%, based on studies on rocks involved in phreatic/hydrothermal explosions (e.g. Mayer et al. 2015, 2016), and a higher porosity of 70% (Table 2).

To simplify the numerical computation and focus on the large-scale eruptive dynamics, we have used the two-phase (i.e. gas plus monodispersed solid particles) version of the Eulerian-Eulerian flow model, which requires the use of a single, hydraulically equivalent grain size and density (Carcano et al. 2014). This can be computed as the first-order moment of the TGSD. According to TGSD calculations (see the "Sample grain-size and total grain-size distribution (TGSD)" section), we selected a single class of ash with a diameter of 1 mm and 2000 kg/m^3 of density to represent the fine material within the erupted mixture. Future studies will address this modelling aspect more specifically. The ballistic component comprises three particle classes, with diameters of 5, 10, and 20 cm, based on field observations. Each particle is modelled as having a constant density of 2500 kg/m^3 and a spherical shape.

Modelling results

The range of initial conditions explored in the simulations revealed scenarios with distinct characteristics. These included the maximum velocity and height reached by the eruptive jet during expansion, maximum ballistic ejection velocity and range, the percentage and timing of column collapse, PDC directionality, and the areas impacted by both PDCs and ballistic fragments. The main quantitative results are summarised in Table 3.

Figure 7 illustrates the evolution of the lower eruptive plume during the first 45 s following the explosion for Runs 1 and 2 ($M = 5 \times 10^7$ kg, $E_m = 12$ kJ/kg; vertical vs. W-inclined vent; Table 2) and Runs 10 and 11 ($M = 1.2 \times 10^7$ kg, $E_m = 12$ kJ/kg; vertical vs. W-inclined vent; Table 2). The simulations captured the generation and propagation of the eruptive mixture, composed of water vapour, ash, and ballistic particles, over time in three-dimensional space. The eruption dynamics involved three main stages: (i) an initial decompression phase (0 to 5–8 s) characterised by the rapid expansion of the eruptive mixture and ballistic acceleration; (ii) a plume formation phase during which the gas-ash mixture was driven vertically by buoyancy, while coarser particles followed quasi-ballistic trajectories (up to 15–20 s); and (iii) a plume collapse and PDCs propagation phase simultaneously with convective plume development. Across these simulations, jet and ballistic properties exhibited minor variations (Table 3), but the dispersal of the eruptive mixture was strongly influenced by the erupted mass and vent orientation. A PDC is formed during the initial expansion phase, with its spreading direction determined by vent orientation. Vertical vents produced PDCs oriented east to north (Fig. 7, Table 3), while W-inclined vents generated PDCs directed northwest to west (Fig. 7, Table 3).

The higher erupted mass runs also displayed a second phase of PDC formation caused by partial plume collapse, occurring approximately 30 s after the explosion onset (Fig. 7). The mass partitioned into convective plumes (F_{Plume}) or collapses, subdivided between mass in PDCs (F_{PDC}) and material settling within the La Fossa crater (F_C), is reported in Table 3. The method for calculating collapse percentages is explained in the Supplementary Information.

Figure 8 shows the variation in collapsing mass percentages over time for selected runs. Collapse percentages were significantly influenced by initial gas pressure and ash volume fraction, whereas vent inclination and geometry (not shown) had a comparatively smaller effect. Higher initial pressures increased mixture ejection velocities (Run 5 in Table 2) and reduced the collapse percentages (Table 3). Conversely, lower pressures and gas volume fractions resulted in higher collapse percentages (Fig. 8, Table 3).

Table 3 Summary of numerical modelling outputs. *ID*, simulation identifier; V_{jet}, maximum velocity of the eruptive jet; H_{jet}, maximum height of the jet above the vent; V_b, maximum ejection velocity of ballistics; R_b, maximum ballistic range; $PDC_{1,2}$, spreading directions of the first and second PDC; F_{PDC}, percentage of material within PDCs; F_C, percentage of material settling within the La Fossa crater; F_{Plume}, percentage of material in the eruptive plume. Bold lettering highlights the simulations that better fit the observed distribution of PDCs and ballistics, as well as the inferred eruption dynamics (see the "Discussion" section)

ID	V_{jet} (m/s)	H_{jet} (m)	V_b (m/s)	R_b (m)	PDC1	PDC2	F_{PDC} (%)	F_C (%)	F_{Plume} (%)
1	190	550	140	700	E	N	21	31	48
2	**190**	**550**	**140**	**900**	**NW**	**W**	**22**	**22**	**56**
3	190	650	140	1000	NW	N	17	12	71
4	**180**	**700**	**140**	**800**	**NW**	**W**	**20**	**40**	**40**
5	230	700	180	1200	N	NE	7	17	76
6	140	550	100	600	NW	-	53	35	12
7	120	550	94	400	W, NW	-	38	60	2
8	190	650	150	900	N	W	9	8	83
9	200	750	160	900	NW, W	W, E	35	6	59
10	180	550	130	600	N	-	6	18	76
11	**180**	**550**	**130**	**700**	**NW, N**	**-**	**11**	**13**	**75**
12	180	500	130	900	NNW	-	17	10	73
13	**100**	**400**	**84**	**300**	**NW, W**	**-**	**47**	**52**	**1**

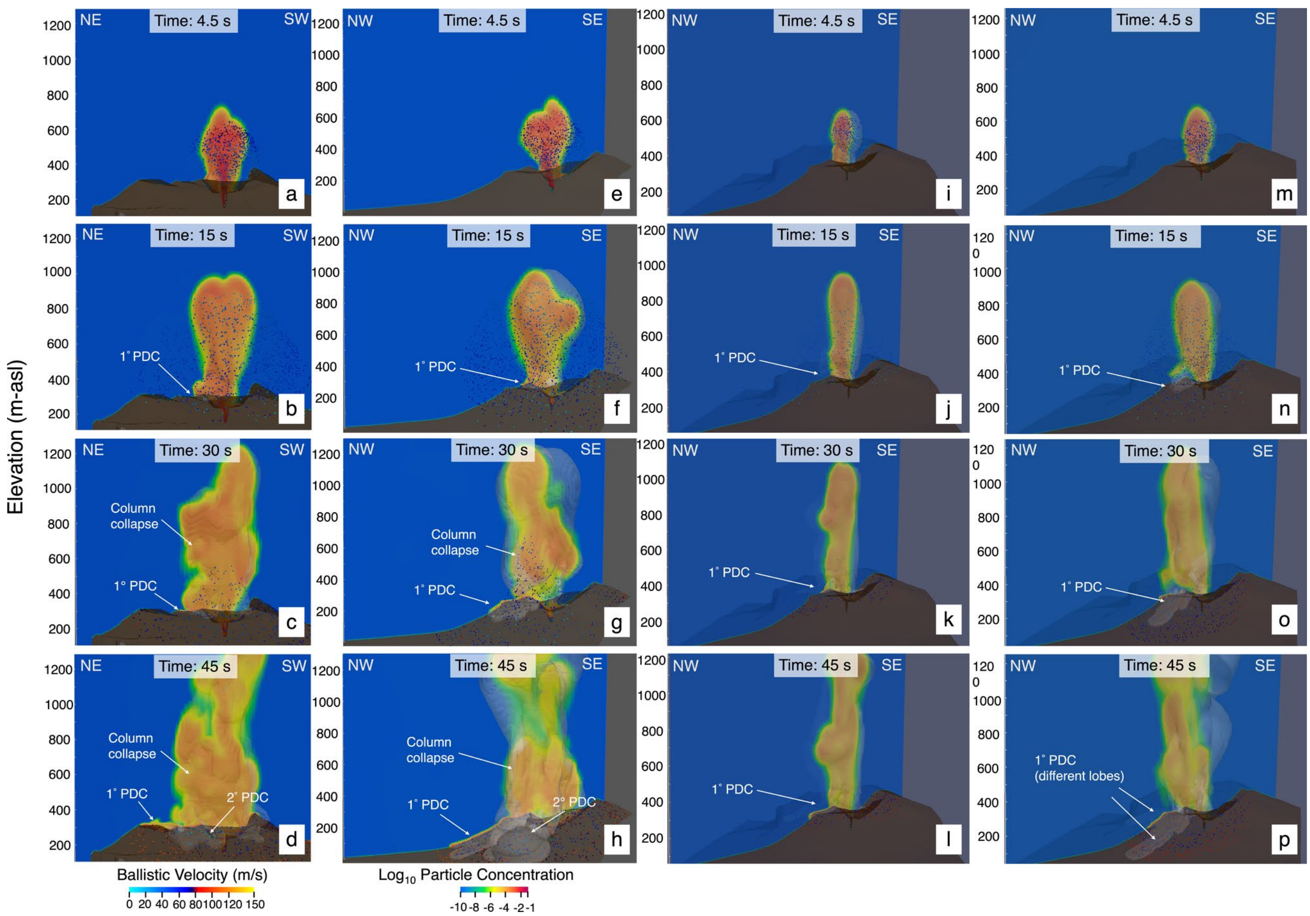

Fig. 7 Evolution over time and space of the gas-particle mixture: **a–d** Run 1 (vertical vent, $M = 5 \times 10^7$ kg); **e–h** Run 2 (W-inclined vent, $M = 5 \times 10^7$ kg); **i–l** Run 10 (vertical vent, $M = 1 \times 10^7$ kg); **m–p** Run 11 (W-inclined vent, $M = 1 \times 10^7$ kg). The 10^{-6} isosurface of particle volume fraction is also shown (shaded grey)

Initial temperature (Run 8 in Table 2) had a more limited impact, mainly enhancing mixture buoyancy and decreasing the collapse percentage (Table 3).

PDC-affected areas for runs with varying vent geometry and orientation (Runs 1–4, 10–12) are shown in Fig. 9. PDCs from vertical vents typically spread north to east, whereas W- or NW-inclined vents directed PDC northwest to west. In these cases (i.e., Runs 2, 4, 11), the areal dispersion of erupted material more closely agreed with the observed BDF distribution in the field compared to vertical vent scenarios (i.e., Runs 1, 10).

Finally, Fig. 10 displays the areas affected by ballistic fallout, with particle distribution represented as the logarithm of the percentage of particles reaching a single pixel. Ballistic distribution was mainly influenced by vent geometry, erupted mass, and explosion energy. Vent inclination produced asymmetrical ballistic dispersal, while higher erupted mass, initial pressure, and gas volume fraction extended ballistic ranges. Ballistic landing times averaged around 30 s but decreased with lower erupted mass and gas volume fractions. Coarser ballistics (20 cm) travelled farther than finer ones (5–10 cm) due to their greater inertia, allowing them to reach greater distances from the eruptive vent.

Discussion

Nature and emplacement mechanisms of the BDF deposits

The absence of juvenile material, combined with the abundance of variably hydrothermally altered material in the deposit, supports the phreatic nature of the eruption responsible for the BDF deposition. As already observed by Mercalli (Mercalli and Silvestri 1891), we suggest that the eruption initiated an eruptive crisis that culminated 15 years after in the 1888–1890 Vulcanian eruption of La Fossa. Similar prolonged crises, in which magma arrival at the surface is heralded by repeated phreatic activity, are quite common also at other volcanoes (see below),

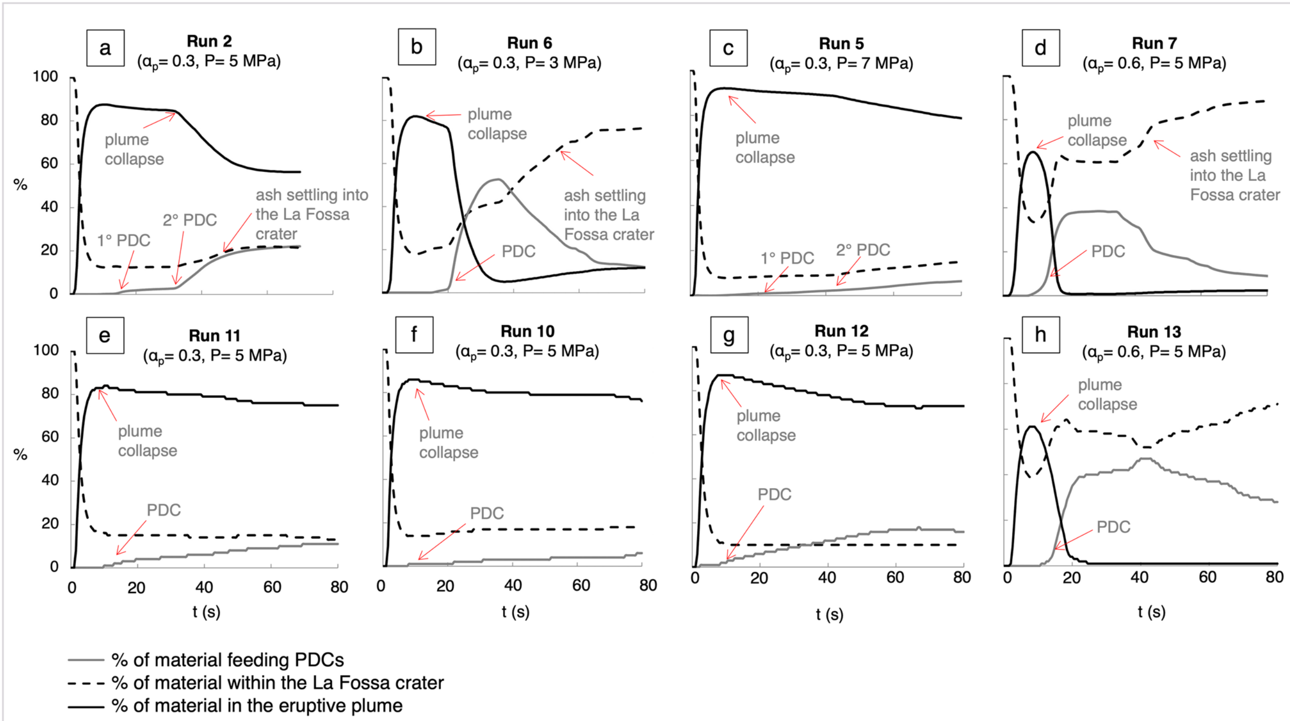

Fig. 8 Graphs showing the collapse percentage over time for **a** Run 2 (W-inclined vent, $M=5\times10^7$ kg); **b** Run 6 ($P=3$ MPa, $M=5\times10^7$ kg); **c** Run 5 ($P=7$ MPa, $M=5\times10^7$ kg); **d** Run 7 (particle volume fraction, α_p, of 0.6, $M=1\times10^8$ kg); **e** Run 11 (W-inclined vent, $M=1\times10^7$ kg); **f** Run 10 (vertical vent, $M=1\times10^7$ kg); **g** Run 12 (NW-inclined vent, $M=1\times10^7$ kg); **h** Run 13 (particle volume fraction, α_p, of 0.6, $M=2.6\times10^7$ kg)

especially in the presence of slowly ascending, highly evolved, viscous magma typical of Vulcanian activity.

Dispersal and sedimentological data give important hints on the explosive and deposition dynamics. The different layers of BDF could be correlated along the north-western flank of the La Fossa cone, and they are confined between elevations of 55–210 m. The sedimentological features, such as massive, matrix-supported portions (indicative of high sedimentation rates from a poorly sorted bed load) alternated with faintly laminated portions (reflecting deposition from a traction-dominated, low-concentration flow boundary), suggest unsteady deposition (Branney and Kokelaar 2002) during rapid aggradation of ephemeral turbulent PDCs. Such features are interpreted to record oscillations in flow velocity and current bulk density during transport and deposition and are well evident at the more proximal sites. These variations, observed in natural PDCs and large-scale experiments (Brosch et al. 2021), appear unrelated to source activity but rather to flow dynamics in the near-vent area. Key characteristics of the BDF layers include irregular thicknesses influenced by local topographic effects, sharp interlayer contacts, and occasional reverse grading indicative of kinematic sieving processes within the bed load. The more complex internal texture of the single layers at proximal sites, where flow dynamics are more turbulent, is in agreement with the proposed interpretation.

Layers A, C, and D also exhibit alignments of blocks to lapilli-sized lithics, often displaying an openwork texture where larger particles are in direct contact, with no finer matrix filling the voids. These features are interpreted as evidence of ballistic showers, indicating simultaneous ballistic deposition during the eruption.

Despite syn- and post-emplacement remobilisation processes can be important in this type of deposits, due to the turbulence of the PDCs and the steepness of the slope, the textural and compositional similarities observed between the single layers at different sites suggest these processes, if present, only played a minor role in the final deposition. A major role of post-depositional erosion and reworking is instead evident at the outcrops closer to the vent area, where the upper layers are often missing (Sects. 22, 10, 9) or at the foot of the cone (Sect. 14).

The cohesive and vesicular matrix of layer E suggests a distinct emplacement mechanism compared to the other layers. These features likely result from the incorporation of water, which increased the cohesiveness and viscosity of the material during deposition, allowing it to trap air bubbles. Based on these characteristics, as well as its massive and poorly sorted nature, we propose that layer E

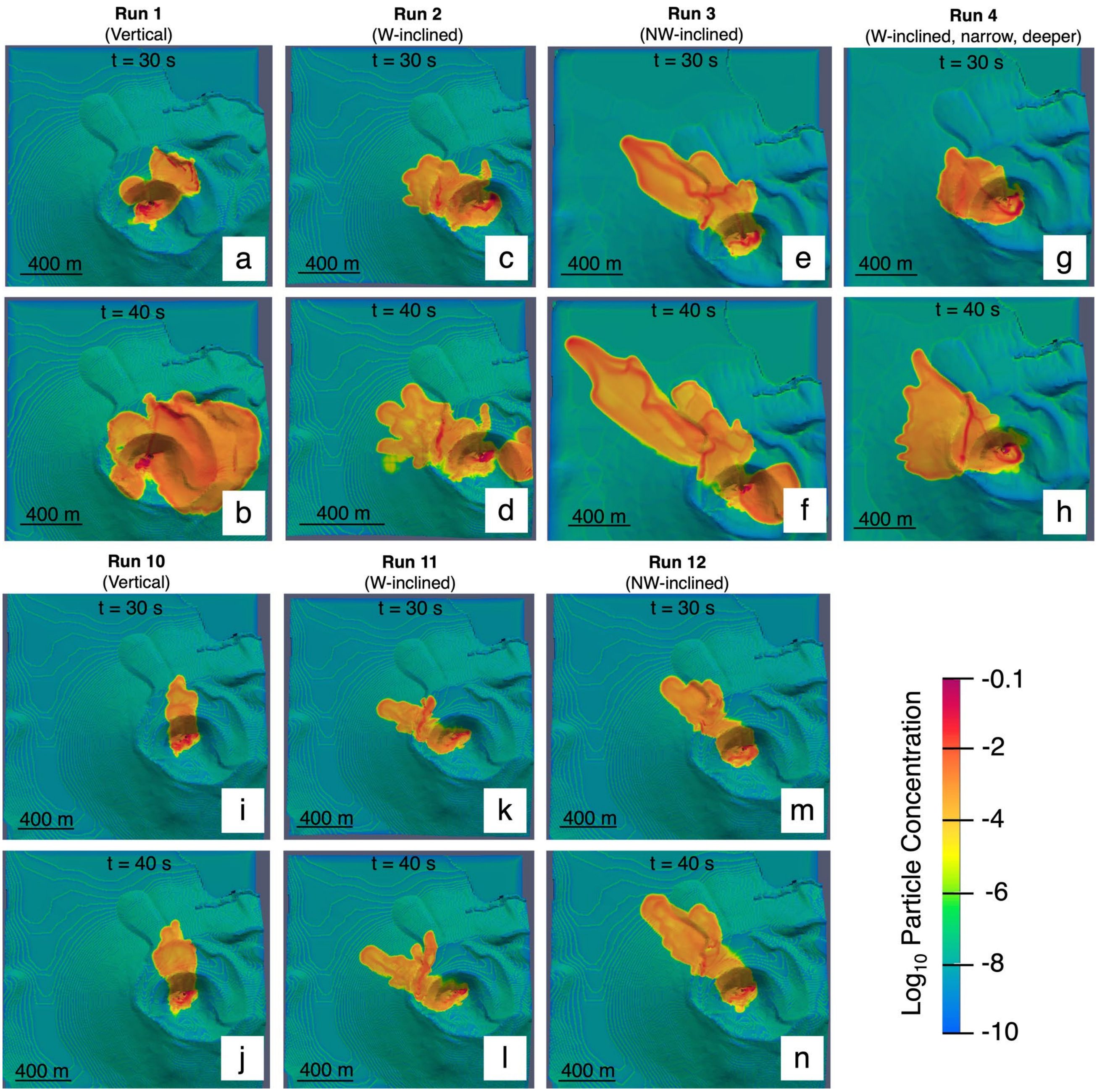

Fig. 9 Top view of the area affected by PDCs under different vent geometries and erupted mass (M): **a**, **b** vertical vent, $M = 5 \times 10^7$ kg (Run 1); **c**, **d** W-inclined vent, $M = 5 \times 10^7$ kg (Run 2); **e**, **f** NW-inclined vent, $M = 5 \times 10^7$ kg (Run 3); **g**, **h** narrow and deeper vent, $M = 4 \times 10^7$ kg (Run 4); **i**, **j** vertical vent, $M = 1 \times 10^7$ kg (Run 10); **k**, **l** W-inclined vent, $M = 1 \times 10^7$ kg (Run 11); **m**, **n** NW-inclined vent (Run 12). Particle concentration on the ground is expressed in logarithmic scale of particle volume fraction

could represent a syn-eruptive lahar. In this scenario, phreatic water interacted with lithic material to form a cohesive flow with properties distinct from a typical pyroclastic suspension. This interpretation is further supported by the strong compositional similarity between layer E and the other BDF layers, as well as its quite consistent thickness and constant presence at the top of the BDF sequence. The phreatic water may have been erupted directly in liquid form during the final stages of the eruption, similar to observations from recent events such as the 2014 Ontake eruption in Japan (Kaneko et al. 2016; Sasaki et al. 2016), or it may have originated from condensed steam.

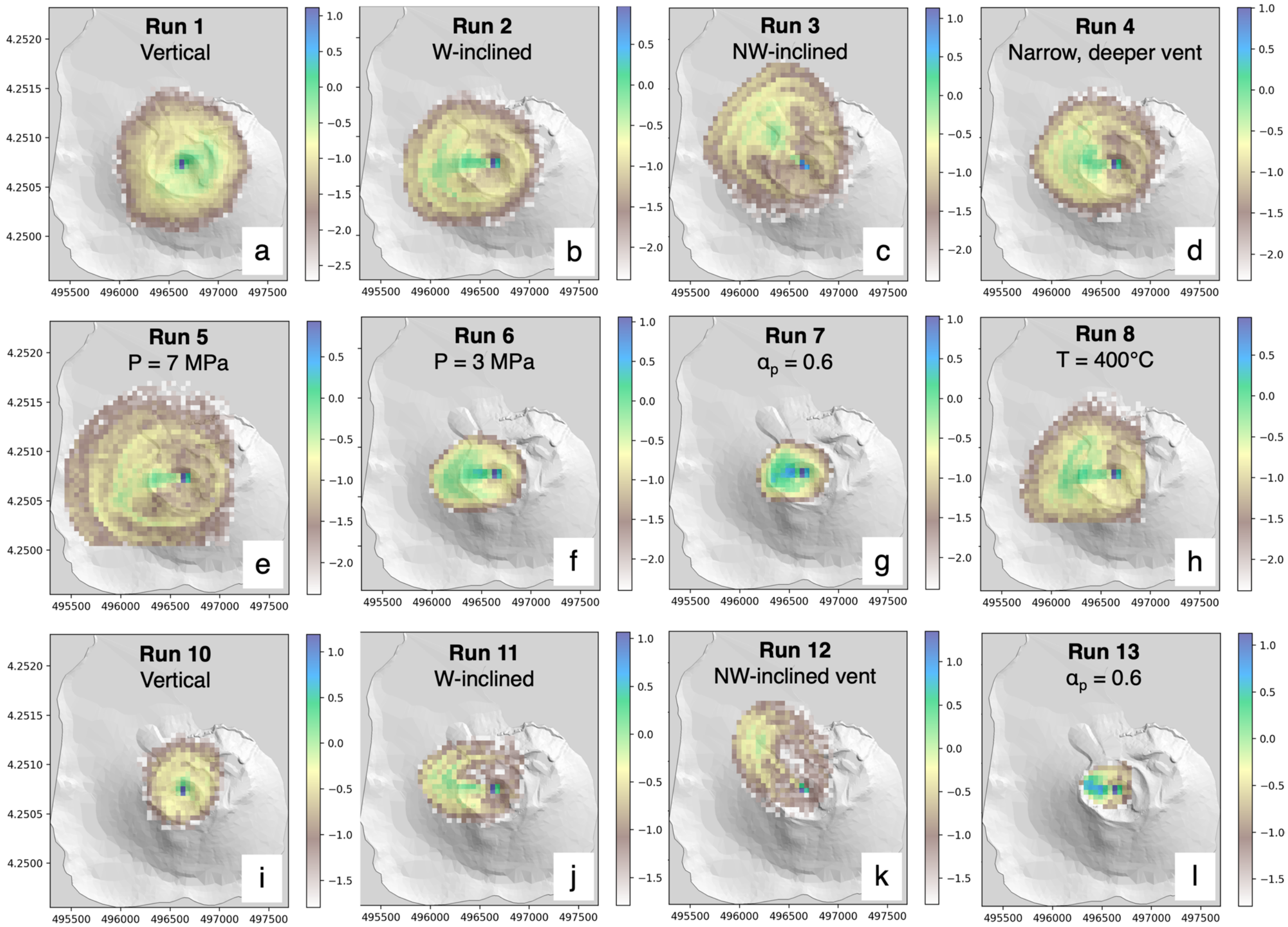

Fig. 10 Map showing the area affected by ballistic fallout (particle diameter of 5, 10, 20 cm). Data are reported as logarithm of the percentage of ballistics: **a** vertical vent, $M = 5 \times 10^7$ kg (Run 1); **b** W-inclined vent, $M = 5 \times 10^7$ kg (Run 2); **c** NW-inclined vent, $M = 5 \times 10^7$ kg (Run 3); **d** narrow and deeper vent, $M = 4 \times 10^7$ kg (Run 4); **e** initial pressure of 7 MPa, $M = 5 \times 10^7$ kg (Run 5); **f** initial pressure of 3 MPa, $M = 5 \times 10^7$ kg (Run 6); **g** particle volume fraction (α_p) of 0.6, $M = 1 \times 10^8$ kg (Run 7); **h** initial temperature of 400 °C, $M = 5 \times 10^7$ kg (Run 8); **i** vertical vent, $M = 1 \times 10^7$ kg (Run 10); **j** W-inclined vent, $M = 1 \times 10^7$ kg (Run 11); **k** NW-inclined vent, $M = 1 \times 10^7$ kg (Run 12); **l** particle volume fraction (α_p) of 0.6, $M = 2.6 \times 10^7$ kg (Run 13)

Dynamics of the BDF eruption

The 1873 explosive phase involved multiple explosions occurring at intervals from 30 min to a few days and the opening of four closely spaced vents (< 100–150 m between the easternmost and westernmost vents) inside the Gran Cratere of La Fossa (Mercalli 1883; De Fiore 1922; Mercalli and Silvestri 1891). This configuration indicates lateral migration of explosive activity, with explosions likely spaced far enough apart to form independent vent structures (Valentine et al. 2015). The formation of multiple craters is a well-documented feature of phreatic eruptions worldwide (e.g., Kaneko et al. 2016; Breard et al. 2014).

The homogeneity of the BDF components, as well as the lack of significant internal reworking and important erosional structures between layers, suggests emplacement over a short time interval. Thus, the complex activity described for the 1873 cycle would well support the occurrence of multiple (major) explosions responsible for the emplacement of the stratified deposit described here.

Consistent with interpretations from field observations, numerical simulations demonstrate that the eruption scenarios modelled under the explored initial conditions are able to produce one or more PDC events, accompanied by ballistic fallout impacting the flanks of the cone. The asymmetrical distribution of the BDF observed in the field may be attributed to the proximity of the source vents to the northern wall of the Gran Cratere. Experimental studies have shown that explosions beneath pre-existing crater walls often produce inclined, laterally directed jets towards the opposing wall (Valentine et al. 2015). Run 2, Run 4, and Run 11 from the numerical simulations, modelled with a vent inclined 21° W and positioned close to the northern crater wall of La Fossa, produced PDCs and ballistic fallout distributions consistent with field observations. These scenarios, involving a total ejected mass of 1×10^7 to 5×10^7 kg and a specific explosion energy around 12 kJ/kg, effectively reproduce the asymmetrical distribution patterns observed in the BDF deposit, supporting the hypothesis of vent location and inclined jet dynamics. The value of the specific energy of these simulations is below the lower bound (~ 1×10^7 J/m^3) explored by Montanaro et al. (2021) for explosions driven by the expansion of water vapour. However, consideration of the minimum energy spent for fragmentation (~ 1×10^6 J/m^3; Montanaro et al. 2021) would lead to a comparable specific energy.

Scenarios with 5×10^7 kg of ejected mass, at the higher range estimated for the total BDF deposit, impact a wide area on the north-western and western flanks of the cone, with ballistics reaching distances up to 700 m, that is about 200 m farther than observed in the field survey. A single explosion of this magnitude could produce two PDC phases: the first from the lateral expansion of the mixture, the second from column collapse. This might explain the formation of at least two distinct beds of the BDF sequence, such as layers A and B. However, mass proportions calculated for the two currents (less than 5% for the first current, up to 22% for the other) do not match field observations, as layer A has a larger volume than B (Table 1). Conversely, an erupted mass around 1×10^7 kg, in the range of those calculated for single layers of the BDF, affects a smaller area on the north-western flank of the La Fossa cone, with ballistics up to 500 m of distance, better aligning with field observations. We therefore suggest that, in agreement with field evidence, each layer of the BDF records the products ejected during a single, small explosion. Each explosion might have had different specific energy, influenced by the water vapour available for expansion. Lower gas volume fractions (implying a specific energy as low as 3 J/kg) might better explain the emplacement of the massive, coarse-grained layers A and D. This general reconstruction is clearly sensitive to the original volume and distribution of the deposit, which might have been modified by erosion and remobilisation, as well as the subsequent 1888–1890 activity.

The relatively small mass involved in the whole eruption, together with the mixture and ballistic dynamics, suggests a shallow explosion source, likely not exceeding 150 m depth (in the simulated scenarios). This is consistent with a model of bottom-up explosions driven by pressurisation of fluids at shallow depths following increased heat and gas advection from a deeper reservoir toward the hydrothermal system. This interpretation agrees with historical accounts of increased fumarole activity preceding (of some months) and accompanying the 1873–1888 period, evidenced by continuous, intense degassing in the crater area. Picone, who witnessed the 1873 explosions, described the pre-eruption conditions as characterised by "a gas pressure so strong that the vent could not adequately dissipate it" (De Fiore 1922). Each explosion in 1873 was shortly preceded by repeated strong subterranean noise, likely accompanied by changes in fumarole emissions, suggesting that the system underwent rapid changes preluding eruptive activity (De Fiore 1922).

Comparison with recently observed events

The total volume of the BDF is estimated at 5×10^4 m^3, falling into typical values for phreatic eruptions (Montanaro et al. 2022). Larger events, like the 2014 Ontake and the 2012 Te Maari/Tongariro eruptions, had volumes around 10^5 m^3 (Lube et al. 2014; Breard et al. 2014; Kaneko et al. 2016; Maeno et al. 2016). Smaller eruptions include the 2016 Whakaari/White Island (~ 1.2×10^4 m^3), the 2015 Hakone (~ 10^2 m^3), and the 2018 Kusatsu-Shirane (3.4–4.9×10^4 m^3; Montanaro et al. 2022).

Phreatic eruptions typically produce columns below 10 km in height (Kaneko et al. 2016; Kilgour et al. 2019; Montanaro et al. 2022). Historical accounts from La Fossa di Vulcano in the 1873–1888 period do not mention this parameter. Our simulations suggest columns reach at least 2 km asl, which is the vertical boundary of the domain. However, it is important to remark that the maximum column height is influenced by fine ash content, which was minimal (less than 5 wt.%) in the 1873 Vulcano activity. In turn, the abundance of ash in the mixture is strictly related to the lithology of the rocks involved in the explosion (Montanaro et al. 2022), indicating that column height could vary for explosion of similar energy but different entrained material.

Ballistic fallout and PDCs, responsible for the BDF deposit formation, have been directly observed in other phreatic eruptions, such as the 2016 and 2019 Whakaari/White Island and the 2014 Ontake eruptions (Kaneko et al. 2016; Maeno et al. 2016; Kilgour et al. 2019; Walsh et al. 2019). Depending on event size and topography, phreatic eruption PDCs can travel up to 2.5 km, with velocities generally not exceeding 45 m/s (Nakada et al. 2005; Kaneko et al. 2016; Geshi and Itoh 2018). In our simulations, PDC velocities range from 10 to 25 m/s, with temperatures between 145 and 200 °C. The temperature of phreatic eruption PDCs is generally lower than that associated with magmatic eruptions, often indicated by the absence of charred trees (Kaneko et al. 2016; Geshi and Itoh 2018).

Historical and observational evidence shows that phreatic eruptions can be characterised by multiple explosions as observed in 1873 at La Fossa and other eruptions, such as the 1976/1977 La Soufrière de Guadeloupe (Heiken et al. 1980; Feuillard et al. 1983; Hincks et al. 2014) and Rincón de la Vieja, Costa Rica (Global Volcanism Program 2017, 2023; Battaglia et al. 2019). The occurrence of multiple explosions over a short time period in 1873 can possibly be attributed to the failure of pressurised fluid pockets within the porous or fractured rocks, characterised by significant lateral and/or vertical gradients of permeability. These pockets may activate sequentially as the system undergoes decompression after an explosion in adjacent areas.

Conclusions

Our study sheds light on small-magnitude ($<5.0\times10^7$ kg) phreatic explosions at La Fossa di Vulcano. Through historical records, field-derived data, and 3D numerical modelling, we identified and described the BDF deposits as the result of multiple explosions during the intense 44-day-long explosive phase in 1873.

The characterisation of the stratigraphic sequence provides elements useful to interpret eruption and emplacement dynamics, as well as essential input parameters for simulations (i.e. grain size, volume, dispersal, dynamics). In particular, we have evidence of how small-scale phreatic explosions can generate PDCs and ballistic showers impacting the slopes of the La Fossa and the areas at the base of the cone.

The geometry and orientation of the eruptive vent determine the final distribution of the ejected material, with initial pressure, gas content, and erupted mass influencing eruption dynamics and energetics, thus the relative proportion of the material going into convection or collapse. Simulations of explosions from inclined vents produce asymmetrical deposit distributions consistent with field observations and show that smaller erupted masses may account for the formation of individual layers of the BDF sequence. It is important to remark that the present numerical analysis is limited to the general explosion phenomenology, PDC formation, and ballistic distribution. For more quantitative information on the emplacement dynamics of PDCs, future studies will require higher resolution (below metre scale) near the ground. Further improvements to the numerical model should also consider multiple particle size classes, which would affect PDC dynamics (e.g. Neri et al. 2003; Esposti Ongaro et al. 2020).

Given the proximity of the La Fossa cone to inhabited areas and growing tourism on Vulcano, understanding the conditions leading to them is crucial for hazard assessment and mitigation on the island. Our findings suggest these explosions may be triggered by pressure build-up in shallow porous rocks due to increased and continuous magmatic gas flux. The BDF case shows this process may precede a magmatic eruption by years or decades. However, quantifying the probability of occurrence of these events remains challenging due to the limited knowledge and constraints on related deposits. Further research is therefore necessary to understand and reconstruct the conditions for high-pressure formation in the shallow porous rocks at La Fossa.

Supplementary Information The online version contains supplementary material available at https://doi.org/10.1007/s00445-025-01797-1.

Acknowledgements The authors would thank A. Neri and the members of the INGV working groups during the 2021 Vulcano hydrothermal crisis for their valuable contributions to the discussions on phreatic activity at Vulcano.

Funding Open access funding provided by Istituto Nazionale di Geofisica e Vulcanologia within the CRUI-CARE Agreement. SG was supported by a PhD fellowship founded by the Istituto Nazionale di Geofisica e Vulcanologia—sezione di Pisa, and partly by the Ministero dell'Università e della Ricerca (MUR) through the PRIN "HEATED" grant 2022FAWX8C. RC, MP, and MdMV were supported by the Ministero dell'Università e della Ricerca (MUR) through the PRIN "HEATED" grant 2022FAWX8C. TEO and MdMV were partially supported by the MUR project Pianeta Dinamico—WUnderVul and by the Euro-HPC Joint Undertaking of the European Union, ChEESE-2P project, Grant Agreement No. 101093038.

Data availability All data needed to evaluate the conclusions in the paper are present in the paper and/or in the Supplementary Information.

Declarations

Conflict of interest The authors declare no competing interests.

References

Aiuppa A, Bitetto M, Calabrese S, Delle Donne D, Lages J, La Monica FP, Chiodini G, Tamburello G, Cotterill A, Fulignati P, Gioncada A, Liu EJ, Moretti R, Pistolesi M (2022) Mafic magma feeds degassing unrest at Vulcano Island. Italy Commun Earth Environ 3:255. https://doi.org/10.1038/s43247-022-00589-1

Badalamenti B, Gurrieri S, Hauser S, Parello F, Valenza M (1988) Soil CO_2 output in the island of Vulcano during the period 1984–1988: surveillance of gas hazard and volcanic activity. Rend Soc It Miner Petrol 43:893–899

Badalamenti B, Gurrieri S, Hauser S, Parello F, Valenza M (1991) Changes in the soil CO_2 output at Vulcano island during the summer 1988. Acta Vulcanol 1:219–221

Barberi F, Neri G, Valenza M, Villari L (1991) 1987–1990 unrest at Vulcano. Acta Vulcanol 1:95–106

Battaglia A, de Moor JM, Aiuppa A, Avard G, Bakkar H, Bitetto M, Mora Fernández MM, Kelly P, Giudice G, Delle Donne D, Villalobos H (2019) Insights into the mechanisms of phreatic eruptions from continuous high frequency volcanic gas monitoring: Rincón de la Vieja volcano. Costa Rica Front Earth Sci 6:247. https://doi.org/10.3389/feart.2018.00247

Bonadonna C, Frischknecht C, Menoni S, Romerio F, Gregg CE, Rosi M, Biass S, Asgary A, Pistolesi M, Guobadia D, Gattuso A, Ricciardi A, Cristiani C (2021) Integrating hazard, exposure, vulnerability and resilience for risk and emergency management in a volcanic context: the ADVISE model. J Appl Volcanol 10(1):7. https://doi.org/10.1186/s13617-021-00108-5

Boyce AJ, Fulignati P, Sbrana A, Fallick AE (2007) Fluids in early stage hydrothermal alteration of high-sulfidation epithermal systems: a view from the Vulcano active hydrothermal system (Aeolian Islands, Italy). J Volcanol Geother Res 166:76–90. https://doi.org/10.1016/j.jvolgeores.2007.07.005

Branney MJ, Kokelaar BP (2002) Pyroclastic density currents and the sedimentation of ignimbrites. Geol Soc Lond 27. https://doi.org/10.1144/GSL.MEM.2003.027

Breard ECP, Lube G, Cronin SJ, Fitzgerald R, Kennedy B, Scheu B, Montanaro C, White JDL, Tost M, Procter JN, Moebis A (2014) Using the spatial distribution and lithology of ballistic blocks to interpret eruption sequence and dynamics: August 6 2012 Upper Te Maari eruption, New Zealand. J Volcanol Geoth Res 286:373–386. https://doi.org/10.1016/j.jvolgeores.2014.03.006

Brosch E, Lube G, Cerminara M, Esposti Ongaro T, Breard ECP, Dufek J, Sovilla B, Fullard L (2021) Destructiveness of pyroclastic surges controlled by turbulent fluctuations. Nat Commun 12:7306. https://doi.org/10.1038/s41467-021-27517-9

Browne PRL, Lawless JV (2001) Characteristics of hydrothermal eruptions, with examples from New Zealand and elsewhere. Earth Sci Rev 52(4):299–331. https://doi.org/10.1016/S0012-8252(00)00030-1

Capaccioni B, Coniglio S (1995) Varicolored and vesiculated tuffs from La Fossa volcano, Vulcano Island (Aeolian Archipelago, Italy): evidence of syndepositional alteration processes. Bull Volcanol 57:61–70. https://doi.org/10.1007/BF00298708

Capasso G, Federico C, Madonia P, Paonita A (2014) Response of the shallow aquifer of the volcano-hydrothermal system during the recent crises at Vulcano Island (Aeolian Archipelago, Italy). J Volcanol Geotherm Res 273:70–80. https://doi.org/10.1016/j.jvolgeores.2014.01.005

Carcano S, Esposti Ongaro T, Bonaventura L, Neri A (2014) Influence of grain-size distribution on the dynamics of underexpanded volcanic jets. J Volcanol Geoth Res 285:60–80. https://doi.org/10.1016/j.jvolgeores.2014.08.003

Chiodini G, Cioni R, Marini L, Panichi C (1995) Origin of the fumarolic fluids of Vulcano Island, Italy and implications for volcanic surveillance. Bull Volcanol 57:99–110. https://doi.org/10.1007/BF00301400

Clarke AB, Esposti Ongaro T, Belousov A (2015) Vulcanian eruptions. The Encyclopedia of Volcanoes, Elsevier, pp 505–518. https://doi.org/10.1016/B978-0-12-385938-9.00028-6

Costa S, Masotta M, Gioncada A, Pistolesi M, Bosch D, Scarlato P (2020) Magma evolution at La Fossa volcano (Vulcano Island, Italy) in the last 1000 years: evidence from eruptive products and temperature gradient experiments. Contrib Mineral Petrol 175:31. https://doi.org/10.1007/s00410-020-1669-0

De Fiore O (1922) Vulcano (Isole Eolie). Rivista Vulcanologica Suppl 3:1–393

De Astis G, Lucchi F, Dellino P, La Volpe L, Tranne CA, Frezzotti ML, Peccerillo A (2013) Geology, volcanic history and petrology of Vulcano (central Aeolian archipelago). JGS Memoirs 37:281–349. https://doi.org/10.1144/m37.11

de' Michieli Vitturi M (2024) OpenPDAC (1.2.0). Zenodo. https://doi.org/10.5281/zenodo.14160640

de' Michieli Vitturi M, Neri A, Esposti Ongaro T, Lo Savio S, Boschi E (2010) Lagrangian modeling of large volcanic particles: application to Vulcanian explosions. J Geophys Res 115, B8. https://doi.org/10.1029/2009JB007111

Dellino P, De Astis G, La Volpe L, Mele D, Sulpizio R (2011) Quantitative hazard assessment of phreatomagmatic eruptions at Vulcano (Aeolian Islands, Southern Italy) as obtained by combining stratigraphy, event statistics and physical modelling. J Volcanol Geother Res 201(1–4):364–384. https://doi.org/10.1016/j.jvolgeores.2010.06.009

Di Giuseppe M, Isaia R, Troiano A (2023) Three-dimensional magnetotelluric modeling of Vulcano Island (Eolie, Italy) and its implications for understanding recent volcanic unrest. Sci Rep 13:16458. https://doi.org/10.1038/s41598-023-43828-x

Di Traglia F, Pistolesi M, Rosi M, Bonadonna C, Fusillo R, Roverato M (2013) Growth and erosion: the volcanic geology and morphological evolution of La Fossa (Island of Vulcano, Southern Italy) in the last 1000 years. Geomorphology 194:94–107. https://doi.org/10.1016/j.geomorph.2013.04.018

Di Traglia F, Pistolesi M, Bonadonna C, Rosi M (2024) The last 1100 years of activity of La Fossa caldera, Vulcano Island (Italy): new insights into stratigraphy, chronology, and landscape evolution. Bull Volcanol 86:47. https://doi.org/10.1007/s00445-024-01738-4

Diliberto IS (2021) Cyclic behavior in the fumaroles output detected by direct measurement of temperature of the ground. Eng Proc 5:47. https://doi.org/10.3390/engproc2021005047

Diliberto I, Gurrieri S, Valenza M (2002) Relationships between diffuse CO_2 emissions and volcanic activity on the Island of Vulcano (Aeolian Islands, Italy) during the period 1984–1994. Bull Volcanol 64:219–228. https://doi.org/10.1007/s00445-001-0198-6

Esposti Ongaro T, Clarke AB, Voight B, Neri A, Widiwijayanti C (2012) Multiphase flow dynamics of pyroclastic density currents during the May 18, 1980 lateral blast of Mount St Helens. J Geophys Res 117(6):B06208. https://doi.org/10.1029/2011JB009081

Esposti Ongaro T, Komorowski JC, Legendre Y, Neri A (2020) Modelling pyroclastic density currents from a subplinian eruption at La Soufrière de Guadeloupe (West Indies, France). Bull Volcanol 82:76. https://doi.org/10.1007/s00445-020-01411-6

Federico C, Cocina O, Gambino S, Paonita A, Branca S, Coltelli M, Italiano F, Bruno V, Caltabiano T, Camarda M et al (2023) Inferences on the 2021 ongoing volcanic unrest at Vulcano Island (Italy) through a comprehensive multidisciplinary surveillance network. Remote Sens 15(5):1405. https://doi.org/10.3390/rs15051405

Ferrucci M, Pertusati S, Sulpizio R, Zanchetta G, Pareschi MT, Santacroce R (2005) Volcaniclastic debris flows at La Fossa Volcano (Vulcano Island, southern Italy): insights for erosion behavior of loose pyroclastic material on steep slopes. J Volcanol Geotherm Res 145:173–191. https://doi.org/10.1016/j.jvolgeores.2005.01.013

Feuillard M, Allegre CJ, Brandeis G, Gaulon R, Le Mouel JL, Mercier JC, Pozzi JP, Semet MP (1983) The 1975–1977 crisis of la Soufriere de Guadeloupe (F.W.I.): a still-born magmatic eruption. J Volcanol Geotherm Res 16(3–4):317–334. https://doi.org/10.1016/0377-0273(83)90036-7

Fierstein J, Nathenson M (1992) Another look at the calculation of fallout tephra volumes. Bull Volcanol 54:156–167. https://doi.org/10.1007/BF00278005

Frazzetta G, La Volpe L, Sheridan FM (1983) Evolution of the Fossa cone, Vulcano. J Volcanol Geother Res 17:329–360. https://doi.org/10.1016/0377-0273(83)90075-6

Frazzetta G, Gillot PY, La Volpe L, Sheridan MF (1984) Volcanic hazards at Fossa of Vulcano: data from the last 6,000 years. Bull Volcanol 47:105–124. https://doi.org/10.1007/BF01960543

Froggatt PC (1982) Review of methods of estimating rhyolitic tephra volumes; applications to the Taupo Volcanic Zone, New Zealand. J Volcanol Geotherm Res 14:301–318
Fulignati P, Sbrana A (1998) Presence of native gold and tellurium in the active high-sulfidation hydrothermal system of the La Fossa volcano (Vulcano, Italy). J Volcanol and Geother Res 86(1–4):187–198. https://doi.org/10.1016/S0377-0273(98)00078-X
Fulignati P, Sbrana A, Clocchiatti R et al (2006) Environmental impact of the acid fumarolic plume of a passively degassing volcano (Vulcano Island, Italy). Environ Geol 49:1139–1155. https://doi.org/10.1007/s00254-005-0158-0
Geshi N, Itoh JI (2018) Pyroclastic density currents associated with the 2015 phreatomagmatic eruption of the Kuchinoerabujima volcano. Earth Planets Space 70(1):1–12. https://doi.org/10.1186/s40623-018-0881-x
Gioncada A, Mazzuoli R, Bisson M, Pareschi MT (2003) Petrology of volcanic products younger than 42 ka on the Lipari-Vulcano complex (Aeolian Islands, Italy): an example of volcanism controlled by tectonics. J Volcanol Geother Res 122(3–4):191–220. https://doi.org/10.1016/S0377-0273(02)00502-4
Global Volcanism Program (2017). Report on Rincon de la Vieja (Costa Rica). In: Crafford AE, Venzke E, (eds) Bulletin of the Global Volcanism Network 42:8. Smithsonian Institution. https://doi.org/10.5479/si.GVP.BGVN201708-345020
Global Volcanism Program (2023) Report on Rincon de la Vieja (Costa Rica). In: Bennis KL, Andrews B (eds) Bulletin of the Global Volcanism Network. Smithsonian Institution pp 48–7
Gurioli L, Zanella E, Gioncada A, Sbrana A (2012) The historic magmatic-hydrothermal eruption of the Breccia di Commenda, Vulcano, Italy. Bull Volcanol 74:1235–1254. https://doi.org/10.1007/s00445-012-0590-4
Harris A, Alparone S, Bonforte A, Dehn J, Gambino S, Lodato L, Spampinato L (2012) Vent temperature trends at the Vulcano Fossa fumarole field: the role of permeability. Bull Volcanol 74:1293–1311. https://doi.org/10.1007/s00445-012-0593-1
Heiken G, Crowe B, Mcgetchin T, West F, Eichelberger J, Peterson R, Wohletz K (1980) Phreatic eruption clouds: the activity of La Soufrière de Guadeloupe, F.W.I., August – October, 1976. Bull Volcanol 43, 383–395. https://doi.org/10.1007/BF02598039
Hincks TK, Komorowski JC, Sparks SR et al (2014) Retrospective analysis of uncertain eruption precursors at La Soufrière volcano, Guadeloupe, 1975–77: volcanic hazard assessment using a Bayesian Belief Network approach. J Appl Volcanol 3:3. https://doi.org/10.1186/2191-5040-3-3
Inguaggiato S, Vita F, Diliberto IS, Mazot A, Calderone L, Mastrolia A, Corrao M (2022) The extensive parameters as a tool to monitoring the volcanic activity: the case study of Vulcano Island (Italy). Remote Sens 14:1283. https://doi.org/10.3390/rs14051283
Kaneko T, Fukashi M, Setsuya N (2016) 2014 Mount Ontake eruption: characteristics of the phreatic eruption as inferred from aerial observations. Earth Planet Sp 68:72. https://doi.org/10.1186/s40623-016-0452-y
Keller J (1980) The Island of Vulcano. Rend Soc It Mineral Petrol 36(1):369–414
Kilgour G, Gates S, Kennedy B, Farquhar A, McSporran A, Asher C (2019) Phreatic eruption dynamics derived from deposit analysis: a case study from a small, phreatic eruption from Whakāri/White Island, New Zealand. Earth Planet Space 71:36. https://doi.org/10.1186/s40623-019-1008-8
Koyaguchi T, Scheu B, Mitani NK, Melnik O (2008) A fragmentation criterion for highly viscous bubbly magmas estimated from shock tube experiments. J Volcanol Geotherm Res 178:58–71. https://doi.org/10.1016/j.jvolgeores.2008.02.008
Lube G, Breard ECP, Cronin SJ, Procter JN, Brenna M, Moebis A, Pardo N, Stewart RB, Jolly A, Fournier A (2014) Dynamics of surges generated by hydrothermal blasts during the 6 August 2012 Te Maari eruption, Mt Tongariro, New Zealand. J Volcanol Geoth Res 286:348–366. https://doi.org/10.1016/j.jvolgeores.2014.05.010
Maeno F, Nakada S, Oikawa T, Yoshimoto M, Komori J, Ishizuka Y, Takeshita Y, Shimano T, Kaneko T, Nagai M (2016) Reconstruction of a phreatic eruption on 27 September 2014 at Ontake volcano, central Japan, based on proximal pyroclastic density current and fallout deposits. Earth Planet Sp 68:82. https://doi.org/10.1186/s40623-016-0449-6
Mastin LG (1995) Thermodynamics of gas and steam-blast eruptions. Bull Volcanol 57:85–98. https://doi.org/10.1007/BF00301399
Mayer K, Scheu B, Gilg HA, Heap MJ, Kennedy BM, Lavallée Y, Lethambrake M, Dingwell DB (2015) Experimental constraints on phreatic eruption processes at Whakaari (White Island volcano). J Volcanol Geotherm Res 302:150–162. https://doi.org/10.1016/j.jvolgeores.2015.06.014
Mayer K, Scheu B, Montanaro C, Yilmaz TI, Isaia R, Donjá A, Dingwell DB (2016) Hydrothermal alteration of surficial rocks at Solfatara (Campi Flegrei): petrophysical properties and implications for phreatic eruption processes. J Volcanol Geotherm Res 320:128–143. https://doi.org/10.1016/j.jvolgeores.2016.04.020
Mercalli G (1886) La Fossa di Vulcano e lo Stromboli dal 1884 al 1886. Atti Soc It Sci Nat 29(2–3):352–361
Mercalli G, Silvestri O (1891) Le eruzioni dell'isola di Vulcano, incominciate il 3 agosto 1888 e terminate il 22 marzo 1890. Ann Ufficio Centrale Meteorol Geodin Ital 10(4):1–213
Mercalli G (1883) Vulcani e fenomeni vulcanici in Italia (Vol. 3). Milano, Arnaldo Forni
Montanaro C, Scheu B, Cronin SJ, Breard ECP, Lube G, Dingwell DB (2016) Experimental estimates of the energy budget of hydrothermal eruptions; application to 2012 Upper Te Maari eruption, New Zealand. Earth Planet Sci Lett 452:281–294. https://doi.org/10.1016/j.epsl.2016.07.052
Montanaro C, Croninc SJ, Scheu B, Kennedy B, Scott B, Dingwell DB (2021) Host rock variability powers the diversity of steam-driven eruptions. Geophys Res Lett 48:e2020GL089025. https://doi.org/10.1029/2020GL089025
Montanaro C, Mick E, Salas-Navarro J, Caudron C, Cronin SJ, de Moor M, Scheu B, Stix J, Strehlow K (2022) Phreatic and hydrothermal eruptions: from overlooked to looking over. Bull Volcanol 84:64. https://doi.org/10.1007/s00445-022-01571-7
Nakada S, Nagai M, Kaneko T et al (2005) Chronology and products of the 2000 eruption of Miyakejima Volcano, Japan. Bull Volcanol 67:205–218. https://doi.org/10.1007/s00445-004-0404-4
Neri A, Esposti Ongaro T, Macedonio G, Gidaspow D (2003) Multiparticle simulation of collapsing volcanic columns and pyroclastic flows. J Geophys Res 108 (B4). https://doi.org/10.1029/2001JB000508
Paonita A, Federico C, Bonfanti P, Capasso G, Inguaggiato S, Italiano F, Madonia P, Pecoraino G, Sortino F (2013) The episodic and abrupt geochemical changes at La Fossa fumaroles (Vulcano Island, Italy) and related constraints on the dynamics, structure, and compositions of the magmatic System. Geochim Cosmochim Acta 120:158–178. https://doi.org/10.1016/j.gca.2013.06.015
Rosi M, Di Traglia F, Pistolesi M, Esposti Ongaro T, de' Michieli Vitturi M, Bonadonna C (2018) Dynamics of shallow hydrothermal eruptions: new insights from Vulcano's Breccia di Commenda eruption. Bull Volcanol 80(83). https://doi.org/10.1007/s00445-018-1252-y
Salino F (1874) Le Isole Lipari. Bollettino Del Club Alpino Italiano VII I(22):135–181

Sasaki H, Chiba T, Kishimoto H, Naruke S (2016) Characteristics of the syneruptive-spouted type lahar generated by the September 2014 eruption of Mount Ontake Japan. Earth Planet Space 68:141. https://doi.org/10.1186/s40623-016-0516-z

Scheu B, Spieler O, Dingwell DB (2006) Dynamics of explosive volcanism at Unzen volcano: an experimental contribution. Bull Volcanol 69:175–187. https://doi.org/10.1016/j.epsl.2013.10.029

Selva J, Bonadonna C, Branca S, De Astis G, Gambino S, Paonita A, Pistolesi M, Ricci T, Sulpizio R, Tibaldi A, Ricciardi A (2020) Multiple hazards and paths to eruptions: a review of the volcanic system of Vulcano (Aeolian Islands, Italy). Earth-Sci Rev 207:103186. https://doi.org/10.1016/j.earscirev.2020.103186

Spieler O, Kennedy B, Kueppers U, Dingwell DB, Scheu B, Taddeucci J (2004) The fragmentation threshold of pyroclastic rocks. Earth Planet Sci Lett 226:139–148. https://doi.org/10.1016/j.epsl.2004.07.016

Stix J, de Moor JM (2018) Understanding and forecasting phreatic eruptions driven by magmatic degassing. Earth Planet Space 70:83. https://doi.org/10.1186/s40623-018-0855-z

Di Traglia F, Bruno V, Casu F, Cocina O, De Luca C, Giudicepietro F, Macedonio G, Mattia M, Monterroso F, Privitera E, Lanari (2023) Multi-temporal INSAR, GNSS and seismic measurements reveal the origin of the 2021 Vulcano Island (Italy) unrest. Geophys Res Lett 50(24). https://doi.org/10.1029/2023GL104952

Valentine GA, Graettinger AH, Macorps É et al (2015) Experiments with vertically and laterally migrating subsurface explosions with applications to the geology of phreatomagmatic and hydrothermal explosion craters and diatremes. Bull Volcanol 77:15. https://doi.org/10.1007/s00445-015-0901-7

Walsh B, Jolly AD, Proctor JN (2019) Geophysical examination of the 27 April 2016 Whakaari/White Island, New Zealand eruption and its implications for vent physiognomies and eruptive dynamics. Earth Planet Space 71:25. https://doi.org/10.1186/s40623-019-1003-0